THE PLASMA ENVIRONMENT OF URANUS

J. W. BELCHER, R. L. McNUTT, JR., J. D. RICHARDSON
Massachusetts Institute of Technology

R. S. SELESNICK
California Institute of Technology

E. C. SITTLER, JR.
NASA Goddard Space Flight Center

and

F. BAGENAL
University of Colorado

In the course of the Voyager 2 encounter with Uranus, an extended magnetosphere filled with a tenuous plasma was detected. This low-energy plasma consists of protons and electrons, with no significant heavy ion contribution, and with a density in the regions sampled by the spacecraft of at most three electrons per cubic centimeter. The plasma electrons and ions exhibit both a thermal component (with temperatures of tens of eV) and a hot component (with temperatures of a few keV). The thermal ion component is observed both inside and outside an L-shell value near 5, whereas the hot ion and electron component is excluded from the region inside of that L-shell. The source of the thermal component of the plasma is either the planetary ionosphere or the neutral hydrogen corona surrounding Uranus, whereas the hot component is convected in from the magnetotail, with probably an ionospheric source. The Uranian moons do not appear to be a significant plasma source. Day-night asymmetries in the fluxes and spatial distribution of the plasma support theoretical models in which solar-wind-driven convection and planet-driven co-rotation are decoupled at Uranus. This decoupling occurs because of the unique orientations of the planetary spin axis with respect to the solar wind flow direction, and of the magnetic dipole axis with respect to the spin axis. As a result of these orientations, convection penetrates deep into the inner Uranian magnetosphere, sweeping out the magnetospheric plasma on relatively short time scales, and preventing the formation of a dense plasmasphere. The exclusion of hot plasma from the region inside an L-shell value near 5 is thought to be due to the presence of a quasi-steady Alfvén layer, although some features in the inner magnetosphere are more characteristic of a time-dependent injection boundary. There are aspects of the plasma data which cannot be easily explained by either of these models. Uranus also possesses a well-developed magnetotail and plasma sheet similar in many respects to those of the Earth. The bow shock observed inbound is a high Mach number quasi-perpendicular shock and shows detailed structure in the transition region similar to that seen at the Earth. Outbound, there is some evidence for periodic velocity variations in the magnetosheath which may be signatures of reconnection. The outbound magnetosheath also has regions in which large plasma density and flow oscillations occur on a time scale of several minutes.

I. INTRODUCTION

The Voyager 2 encounter with Uranus in January of 1986 revealed a fully developed magnetosphere with a number of novel features. The most striking of these was the large 58°.6 tilt of the magnetic dipole axis with respect to the rotation axis of the planet. In addition, the plasma environment at Uranus exhibited many unexpected properties. These plasma features mark the Uranian magnetosphere as uniquely different from those of Jupiter and Saturn at this epoch. In this review, an overview of the observational results on the plasma environment at Uranus is given, and the implications of those observations for magnetospheric physics at Uranus are discussed. Pre-encounter expectations for this magnetosphere are first reviewed, to highlight the novelty of the subsequent observations. An in-depth discussion of observations in the inner magnetosphere and their theoretical interpretation follows, as it is this region which remains the most perplexing. Properties of the magnetotail and the plasma sheet, the magnetosheath plasma, and the bow shock are then considered. The results presented here are based primarily on observations by the Plasma Science Experiment (PLS) on Voyager 2, which measures ions and electrons in the energy range from 10 V to 5950 V (Bridge et al. 1977; Bridge et al. 1986; Selesnick and Richardson 1986; McNutt et al. 1987; Bagenal et al. 1987; Selesnick and McNutt 1987; Sittler et al. 1987; Selesnick 1988).

Pre-Encounter Expectations

Uranus is unique in the solar system in that its rotation axis lies nearly in its orbital plane. The orbital period of Uranus about the Sun is 84 yr, and, in this particular epoch, the Uranian rotation axis lies close to the Sun-planet line. This fortuitous circumstance led to early speculation on the nature of a

possible "pole-on" magnetosphere (Siscoe 1970,1975,1978*a;* Kennel 1973; Dryer et al. 1973; Biernat et al. 1981; Voigt et al. 1983; Ip 1984). The discovery of bright ultraviolet emission from the planet by the International Ultraviolet Explorer (IUE) (Clarke 1982; Durrance and Moos 1982) in 1982 led to the hypothesis that charged-particle excitation of H and H_2 were responsible for the emissions and indicative of auroral processes. A number of workers developed magnetospheric models capable of explaining the auroral emissions; these models predicted surface equatorial field strengths of ~4 G (Hill et al. 1983; Hill and Dessler 1985; Ip and Voigt 1985). In addition, there was some debate as to the importance of the Uranian moons as sources of magnetospheric plasma (Cheng 1984; Hill 1984; Cheng and Hill 1984; Eviatar and Richardson 1986).

These magnetospheric speculations were tempered in 1984 by Desch and Kaiser (1984), who formulated a "radiometic Bode's law" based on the strength of the radio emissions of Earth, Jupiter and Saturn as compared to the strength of their magnetic fields. Using this law, they predicted at what point such emission should be observed by the Voyager 2 Planetary Radio Astronomy (PRA) experiment, as a function of distance from the planet and the strength of the Uranian magnetic field. As Voyager neared the planet in late 1985 with no detection of nonthermal radio emission, these authors placed increasingly restrictive upper limits on the possible magnetic dipole strength of Uranus (Kaiser et al. 1985). In addition, an alternate interpretation of the ultraviolet emission seen by IUE was advanced by Shemansky and Smith (1986) in terms of a phenomenon known as electroglow. Electroglow is a poorly understood process which previously had been observed at Jupiter and Saturn. Both of these planets show high altitude excitation of atomic hydrogen in the sunlit atmospheres, extending well into the exospheric region. Most of the H Lyman α emission in each case is caused by the direct excitation of atomic hydrogen by electrons. The process is apparently catalyzed by solar radiation, but the energy deposition rate far exceeds the solar input. The energy source is unknown but is not magnetospheric in origin and is instead related to an unknown internal process at the planets themselves (see chapter by Strobel et al.).

If this process also occurred at Uranus, Shemansky and Smith (1986) pointed out that this would explain the IUE observations without the need for a magnetospheric interpretation. Furthermore, the lower gravitational field of Uranus, compared to Jupiter and Saturn, would have significant consequences in terms of a possible neutral hydrogen corona surrounding Uranus. The electron impact dissociation of molecular hydrogen and subsequent reactions produces an atomic product with substantial kinetic energy. At Jupiter the dissociation products all appear to be below the escape energy. At Saturn, about 10% of these particles are above the escape energy, and at Uranus the escape fraction is about 80%. The interpretation of the ultraviolet emissions as electroglow proved to be essentially correct at the time of the encounter (Broadfoot et al. 1986), although there is a substantial planetary magnetic field. The associated prediction of an extended hydrogen corona was also borne out. In addition to the lack of detection of radio emission and the alternate explanation for the ultraviolet emission, further IUE studies of the strength of the ultraviolet emission showed that it was uncorrelated with the solar wind energy flux as extrapolated from Voyager 2 and Pioneer 11 (Clarke et al. 1986). Thus, as Voyager 2 approached Uranus in late 1985 with no detection of radio emission, there was increasing speculation that Uranus would not have a magnetosphere (Kaiser et al 1985). One model which retained the expectation of a magnetosphere but with a radio-quiet day side was suggested by Curtis (1985), who predicted classic nonthermal radio emission from the night side of Uranus, but highly suppressed emission from the day side, because of the unique orientation of the rotation axis.

The pre-encounter expectations for the low-energy plasma environment at Uranus were based on experience in the magnetospheres of Jupiter and Saturn. The classic calculation for the distance to the plasmapause (see, e.g., Brice and Ioannidis 1970; Hill 1984) for solar wind conditions at 20 AU and for a reasonable magnetic dipole moment of the planet (using a "magnetic Bode's law" to estimate the magnetic field of Uranus) yields a plasmapause distance which extends beyond the magnetopause on the day side. Thus the magnetosphere of Uranus was predicted to be co-rotation dominated, as at Jupiter and Saturn, instead of convection-dominated, as at Earth; that is, the plasma in the inner and middle magnetosphere would be co-rotating with the planet, and shielded from sunward flow driven by the solar wind. The major contributor to the plasma population was envisaged to be heavy ions produced by sputtering from the icy satellites. These ions would form co-rotating plasma tori at Uranus similar to those seen at Saturn (i.e., consisting of the dissociation products of H_2O). The ionosphere of the planet and the solar wind would be less important contributors (Cheng 1984; Eviatar and Richardson 1986). As at Jupiter and Saturn (Belcher 1983; Lazarus and McNutt 1983; Richardson 1986), it was expected that the thermal speed of the plasma in the PLS energy range would be comparable to or smaller than the local co-rotation speed, i.e., the plasma would be transonic or supersonic with respect to local co-rotation speeds. This situation is a natural result of local pick-up and radiative cooling of ions freshly ionized from neutrals. Consequently, deep inside the inner magnetosphere the plasma was expected to be confined reasonably closely to either the magnetic equator or to the centrifugal equator. The centrifugal equator is intermediate between the rotational and magnetic equators (Hill et al 1974). In any case, in the inner magnetosphere, the plasma was expected to exhibit a spatial distribution little influenced by the solar wind.

With the above scenario, one of the major concerns in encounter planning was whether co-rotating plasma would be sufficiently energetic to be detected above the 10 V threshold of the PLS instrument. For a pre-encounter

estimate of the Uranian rotation period of 15 to 18 hr, the rigid co-rotation speed is ~2.6 km s^{-1} times the distance from the rotation axis in R_U. The energy of a co-rotating ion is then ~0.035 eV times its mass (in units of the proton mass) times the square of the distance from the rotation axis. Because of the orientation of the rotation axis of the planet with respect to the encounter trajectory, the spacecraft is never far from the rotation axis of Uranus in the inner magnetosphere (cf. Fig. 1), and co-rotational energies along the spacecraft trajectory at a typical distance of 5 R_U are only of order 1 eV for protons and 16 eV for O^+. Thus, the expectation was that the PLS instrument would be unable to detect transonic or supersonic co-rotating protons because of the 10 V threshold of the instrument. Similarly, it was expected that transonic or supersonic O^+ would be detected only in the first few energy-per-charge channels of the instrument, and only if the spacecraft were oriented so that one of the PLS sensors was looking as closely into the co-rotating flow direction as possible. Owing to the expectation that the plasma would be concentrated near the equatorial plane, encounter planning emphasized a spacecraft roll orientation around the crossing of the equatorial plane (or ring plane) which put the D-sensor of the PLS instrument looking as closely as possible into the co-rotation direction to allow the detection of O^+. Even with

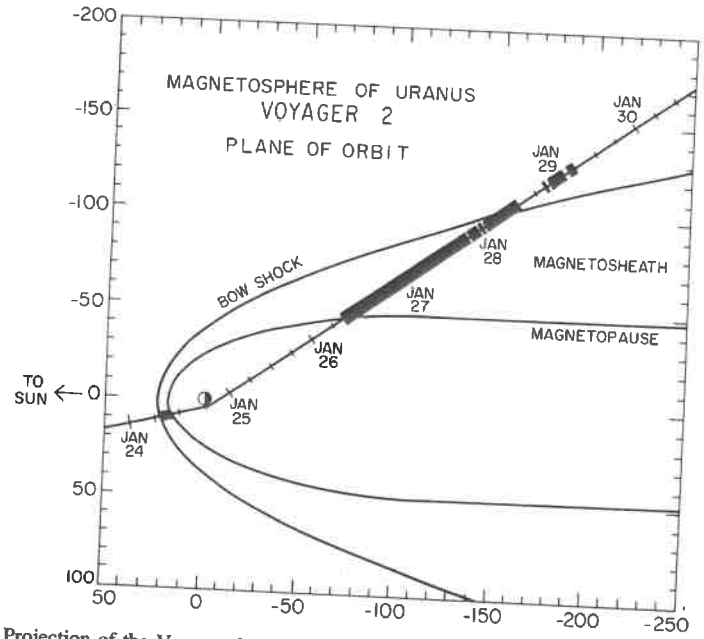

Fig. 1. Projection of the Voyager 2 spacecraft trajectory onto the orbital plane of Uranus, with bow shock and magnetopause cross sections modeled from the observed crossings (figure after Bridge et al. 1986). The shading indicates regions where magnetosheath plasma was detected.

this optimal orientation, it was expected that a major fraction of the plasma population at Uranus (i.e., transonic or supersonic cold co-rotating protons) would remain "hidden" below the 10 V instrument threshold.

The Voyager 2 encounter occurred on 24 January 1986, with closest approach at 1759 Universal Time Coordinated (UTC). In the following, times quoted in UTC refer to event time or data collection time at the spacecraft; this time is also referred to as Spacecraft Event Time (SCET). The first detection of radio emission occurred just 5 days before closest approach (Gurnett et al. 1986) and indicated the probable presence of a magnetosphere. The inbound bow shock crossing occurred on January 24 at about 0730 UTC (24 R_U from the planet, where 1 R_U is defined as 25,600 km) with the magnetopause crossing at 1007 UTC (18 R_U from the planet). Figure 1 shows the planet, the spacecraft trajectory, and the location of the various inbound and outbound bow shock and magnetopause crossings. As the spacecraft moved past closest approach and began to view the night side of the planet for the first time, the pre-encounter predictions by Curtis (1985) of an asymmetry in the radio emissions were dramatically confirmed (Warwick et al 1986). Outbound from the planet, the spacecraft detected an Earth-like magnetic tail and associated plasma sheet. A combination of magnetic field and radio observations fixed the rotation rate of the planet at 17.24 hr (Desch et al. 1986).

II. THE INNER MAGNETOSPHERE

The reality of the plasma environment at Uranus was surprisingly different from the pre-encounter expectations. The plasma was found to consist of electrons and subsonic protons, with thermal speeds well above co-rotational speeds and thermal energies well above the 10 V threshold of the Plasma Science instrument. Based on analysis during a period of negative spacecraft charging outbound, there is good evidence that no substantial "hidden" population of cold protons exists in the magnetosphere. There is also no indication of the presence of heavier ions above threshold flux levels, and thus the Uranian moons do not appear to be a significant plasma source. Most surprisingly, the PLS data exhibited pronounced day-night asymmetries deep in the inner magnetosphere. These asymmetries led to the realization (Vasyliunas 1986; Selesnick and Richardson 1986; Hill 1986) that the near alignment of the solar wind velocity and the rotation axis, combined with the large angle between the magnetic dipole axis and the rotation axis, effectively decouples the co-rotation and convection electric fields at Uranus. As a result, solar-wind-driven sunward convection penetrates deep into the magnetosphere. Plasma primarily co-rotates but also moves slowly sunward, so the overall motion is along helical paths from the night side to the day side. This sunward motion is slow compared to co-rotation, but it sweeps out the magnetospheric plasma fast enough to prevent the formation of a dense plasmasphere. The

sunward convection provides a natural explanation for the observed day-night asymmetries.

Spacecraft Trajectory

As a prelude to discussing the observations on which these conclusions are based, we first present representations of the Voyager 2 trajectory in the inner magnetosphere in 3 different coordinate systems. The first of these coordinate systems is based purely on the spatial geometry of the encounter; the remaining 2 systems are based on both the spatial geometry of the spacecraft trajectory and on the magnetic field geometry of the planet. The plasma features indicated on these figures will be discussed subsequently.

Figure 2 shows the trajectory of the spacecraft projected onto the orbital plane of the planet, with the horizontal axis along the planet-sun line. The trajectory of the spacecraft was approximately in this plane. Figure 3 is based on the offset tilted dipole (OTD) magnetic field model of Ness et al. (1986), and shows the trajectory of the spacecraft in magnetic coordinates. The $\mathbf{Z}_M$ axis in these coordinates is the magnetic dipole axis of the planet; the $\mathbf{X}_M$ and the $\mathbf{Y}_M$ axes are axes perpendicular to the $\mathbf{Z}_M$ axis, as defined in more detail in the following. The horizontal axis in Fig. 3 is cylindrical distance of the spacecraft from the magnetic dipole axis. This coordinate system would organize plasma structures in the inner magnetosphere if they were axially symmetric about the magnetic dipole axis. The loop in the trajectory is a result of the large tilt angle between the magnetic and rotation axes of the planet. The spacecraft crossed the magnetic equatorial plane of Uranus at 1319 UTC and remained at north magnetic latitudes for the rest of the period of interest.

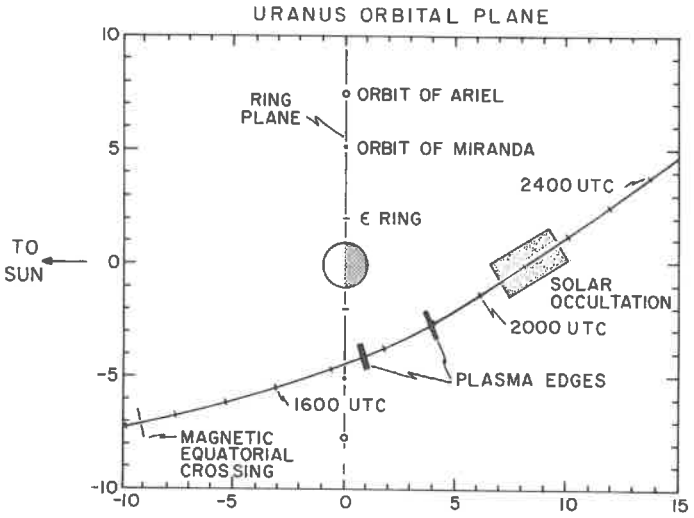

Fig. 2. Trajectory of the Voyager 2 spacecraft projected onto the orbital plane of the planet (slightly different from the plane which contains the trajectory) (figure after McNutt et al. 1987). The horizontal axis points away from the Sun, and the vertical axis points in the direction of Uranus' motion. The locations of the ε ring and of the orbits of Miranda and Ariel are shown, as well as the location of the solar occulation period and the locations of the plasma edges seen in the PLS data.

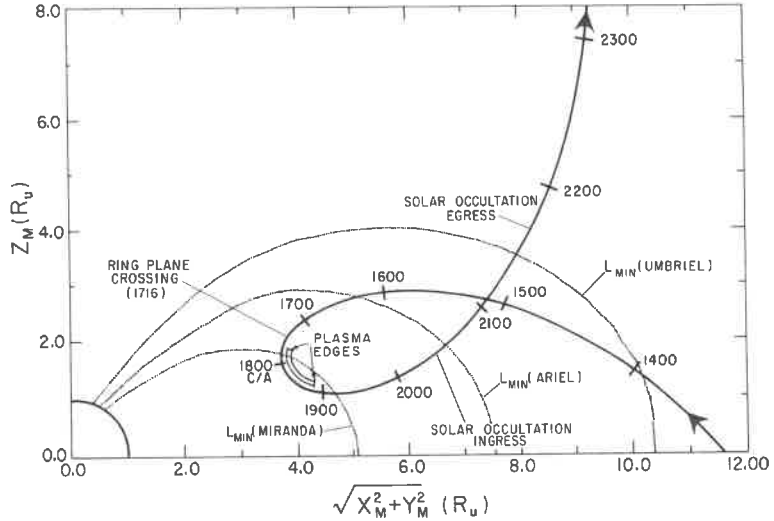

Fig. 3. Trajectory of the Voyager 2 spacecraft in magnetic coordinates corresponding to the OTD model described by Ness et al. (1986) (figure after Bridge et al. 1986). The minimum magnetic L-shells of the satellites Miranda, Ariel and Umbriel are shown. Also indicated are the location of the solar occultation period, and the locations of the plasma edges seen in the PLS data.

Figure 4 is complementary to Fig. 3, and is a projection of the spacecraft position along field lines into the magnetic equator using the OTD model. That is, Fig. 4 is a polar plot of dipole L vs magnetic longitude. The view is from above the north magnetic pole of Uranus. The $\mathbf{Y}_M$ axis in this plot is in the $\boldsymbol{\Omega} \times \mathbf{M}$ direction, where $\boldsymbol{\Omega}$ is the rotational axis of the planet and $\mathbf{M}$ is the magnetic dipole vector. Since $\boldsymbol{\Omega}$ is approximately anti-parallel to the solar wind velocity $\mathbf{V}_{SW}$, the $\mathbf{Y}_M$ direction is close to the $-\mathbf{V}_{SW} \times \mathbf{M}$ direction. As we discuss more fully in the following, this is the direction of the convective electric field needed to drive plasma flow across the polar caps in the direction of solar wind flow (Kavanagh et al. 1968; Selesnick and Richardson 1986). The $\mathbf{Y}_M$ direction in Fig. 4 is analogous to the dawn-dusk direction in the Earth's magnetosphere (that is, the direction of the convection electric field). The minimum L reached by the spacecraft was $L = 4.59$ at 1828 UTC. The actual closest approach to the planet was 4.24 R_U at 1759 UTC (Stone and Miner 1986). Also shown in Fig. 4 are circles of constant L and the regions (shaded portions of the trajectory) where both the hot and intermediate ion components were observed (as described in the following).

The coordinates of Fig. 4 are probably the most appropriate for the PLS

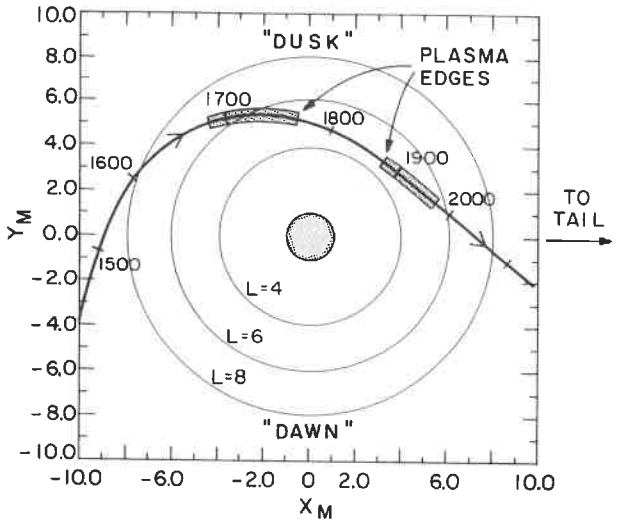

Fig. 4. The trajectory of Voyager 2 projected along dipole magnetic field lines into the magnetic equator, looking from above the north magnetic pole of Uranus (figure after Selsenick and McNutt 1987). The magnetic field points into the plane of the figure. The Y_M axis is in a direction analogous to the dawn-dusk direction in the Earth's magnetosphere (see text). The sense of magnetic gradient drifts for ions is in a counterclockwise direction.

data. For all of the plasma observed by the PLS experiment within the magnetosphere, the inferred thermal energy was much greater than the centrifugal or gravitational potential energy. This implies that if the pressure is isotropic, the density, temperature and pressure should be field-line constants (that is, they should not vary along field lines). Therefore a trajectory plot such as Fig. 4, that uses the two cross-field coordinates, is the most useful with regard to the PLS data because the plasma parameters are expected to vary only across the field lines, and not along them. Even if there is some anisotropy (which the PLS observations cannot rule out), the main variations should still be across the field.

Plasma Instrument Operation

An understanding of the operation of the PLS instrument is necessary to the discussion of the observations. The PLS experiment consists of 4 modulated-grid Faraday cups, each pointing in a different direction (Bridge et al. 1977). The main sensor, consisting of 3 of the cups (A, B and C), pointed toward Earth during the encounter. The side sensor (D cup) pointed in approximately the correct direction for detection of co-rotating, supersonic heavy ions near closest approach to Uranus. Although such ions were not present, the optimal roll attitude of the spacecraft near closest approach helped to characterize the velocity of the subsonic protons that were detected, and this was crucial in the determination of composition, as discussed below.

The PLS instrument measures both electrons and positive ions in the energy-per-charge range from 10 V to 5950 V. Positive ions are collected simultaneously in each of the four Faraday cups with both a low (*L* mode) and high (*M* mode) energy-per-charge resolution. Of the 4 Faraday cups, only the D cup (with its field of view orthogonal to the solar direction) can measure electrons. Electron measurements are made in 2 energy-per-charge ranges, an *E*1 mode with 16 contiguous energy-per-charge channels from 10 V to 140 V, and an *E*2 mode with 12 contiguous energy-per-charge channels from 140 V to 5950 V.

Since Voyager 2 was entering an unknown plasma environment at Uranus, the manner in which the instrument acquired data was reprogrammed during the flight from Saturn to Uranus so as to maximize the information return for a broad range of possible environments. The major change was that the *L*, *E*1 and *E*2 mode measurements at Uranus were made using both a long (960 ms) and a short (240 ms) integration time for each channel, and the *M* mode measurement was made exclusively using the long integration time. During the Jupiter and Saturn encounters, only the short integration time was available, for all modes. The long integration measurement was included to improve the signal-to-noise ratio in the event of a low-density plasma environment, while the short integration measurement was retained to avoid saturation in the event of a high-density plasma environment. Hindsight shows that reprograming to include the long integration time was crucial to the success of the observations at Uranus, because the ambient plasma was in fact tenuous. Most of the PLS results at Uranus are based on these long integration measurements.

The increase in sampling options at Uranus, with no increase in data rate, had the result that the high energy-per-charge resolution *M* mode was sampled less frequently as compared to Jupiter and Saturn. An *M*-mode measurement takes about 2 min and is repeated every 12 min; time aliasing is minimized by telemetering the *M*-mode energy-per-charge scans in one continuous segment from the spacecraft to Earth, instead of in two segments as during the Voyager encounters at Jupiter and Saturn. The *L*, *E*1 and *E*2 long measurements take 15.3 s, while the *L*, *E*1 and *E*2 short measurements take 3.8 s. One *L*-long and one *L*-short spectral set are obtained approximately every 48 s. The *E*1 and *E*2 modes are sampled less frequently, with one long integration and one short integration *E*1/*E*2 pair obtained every 96 s. Additional details of the sampling scheme are given in Sittler et al. (1987, Table 1).

Electron and Positive-ion Distribution Functions

The electron distribution functions measured in the Uranian magnetosphere typically consist of a cold Maxwellian component (T~7 eV to 30 eV) and a hot non-Maxwellian component (T~500 eV to 2 keV). Figure 5 shows representative electron distribution functions in the inner magnetosphere,

demonstrating the presence of these hot and cold components. The parameters n_e and T_e characterize the entire distribution function, and are obtained from moment integrations over that distribution. The parameters n_c and T_c characterize the cold Maxwellian component of the electron distribution function, and are obtained from a Maxwellian fit to the low-energy thermal part of the distribution function, as illustrated in Fig. 5. The parameters n_h and T_h characterize the hot non-Maxwellian part of the electron spectrum, and are obtained from a moment integration over the full distribution function after subtraction of the Maxwellian fit to the cold electrons (see Sittler et al. 1987 and references therein). The breakpoint energy E_B between the cold and hot components shown in Fig. 5 depends on the relative density of the cold and hot electron components.

The positive-ion distribution functions measured in the Uranian magnetosphere exhibit a complex structure that can be described roughly by 3 components; a warm population (T~10 eV), an intermediate population (T~50 to 100 eV) and a hot population (T~700 eV to 3 keV). The designation "warm" is used to imply that thermal energies of the ions significantly exceed co-rotational energies. Figure 6 shows representative ion spectra and Maxwellian fits to those spectra. These are nonlinear least-squares fits to the data, with the full instrument response function included (see McNutt et al. 1987, and references therein). Up to 3 convected Maxwellians have been used to characterize each positive-ion spectrum, depending on which of the warm, intermediate, and hot components were evident (Selesnick and McNutt 1987). For most of the time, the hot and intermediate components appear to be part of a single non-Maxwellian distribution; the use of 2 separate Maxwellian distributions to fit this non-Maxwellian part of the spectrum is simply a way to characterize the full ion distribution function.

The PLS instrument is an electrostatic instrument, so it measures only energy-per-charge. Thus it is not capable of direct measurements of composition. Nonetheless, the positive ions shown in Fig. 6 are thought to be due to protons, and not due to heavy ions. The conclusion that protons are the dominant ionic species in the PLS data is based on the following argument. If it is assumed that the warm component is H^+, then the velocity vector obtained from fits using all of the PLS sensors is consistent with that predicted by rigid co-rotation (as discussed below, the sunward convective motions are too small to be directly observable in the plasma data). Heavier ions (e.g., O^+) could produce only the signatures observed in the low-energy part of the spectra if their velocity vectors are in a very different (nonazimuthal) direction with speeds above the local co-rotation speed. The small amount of dynamical loading of the magnetic field by the plasma (Bridge et al. 1986), consistent with the inferred vacuum magnetic field (Ness et al. 1986), strongly suggests that the plasma is nearly co-rotating with the planet, and this is consistent only with a proton composition. A proton plasma is also consistent with the absence of heavier ions at ~1 MeV per nucleon (Krimigis

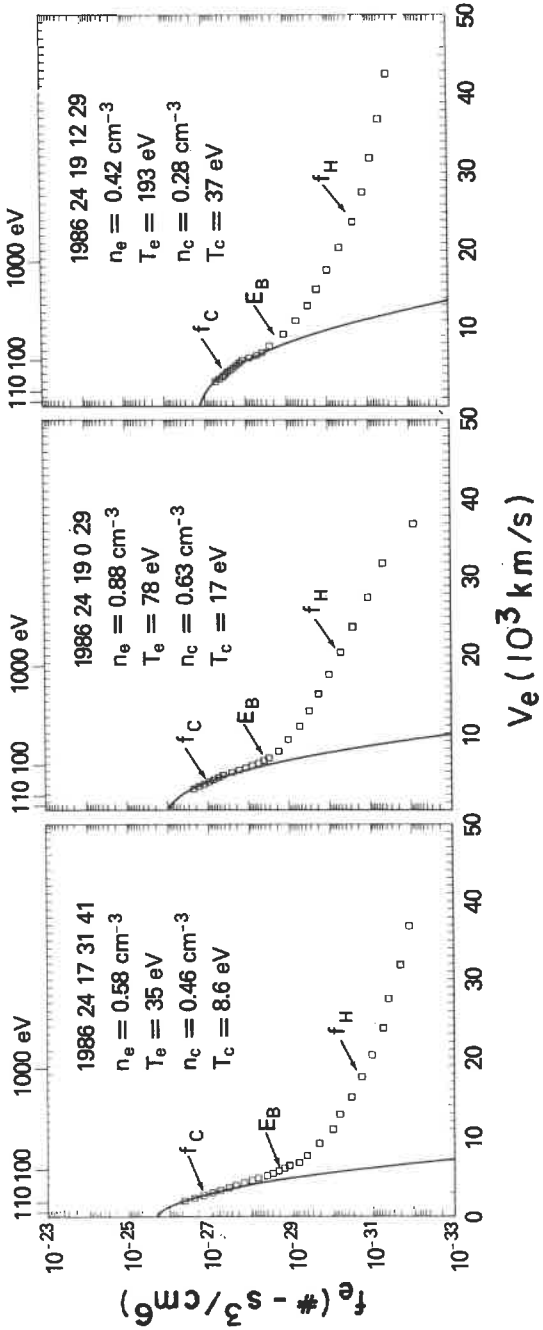

Fig. 5. Examples of electron distribution functions measured by the PLS instrument within the Uranian inner magnetosphere (figure after Sittler et al. 1987). The vertical scale is in number per phase space volume element, the lower horizontal scale is linear in electron speed (in units of 10^3 km s^{-1}), and the upper horizontal scale is energy in eV. The open squares are data points obtained by combining contiguous *E*1 and *E*2 spectra. The solid curve is a Maxwellian fit to the low-energy thermal electrons. Cold and hot electron components are clearly evident. The breakpoint energy E_B between the cold and hot components is dependent on the relative density of the cold and hot electron components.

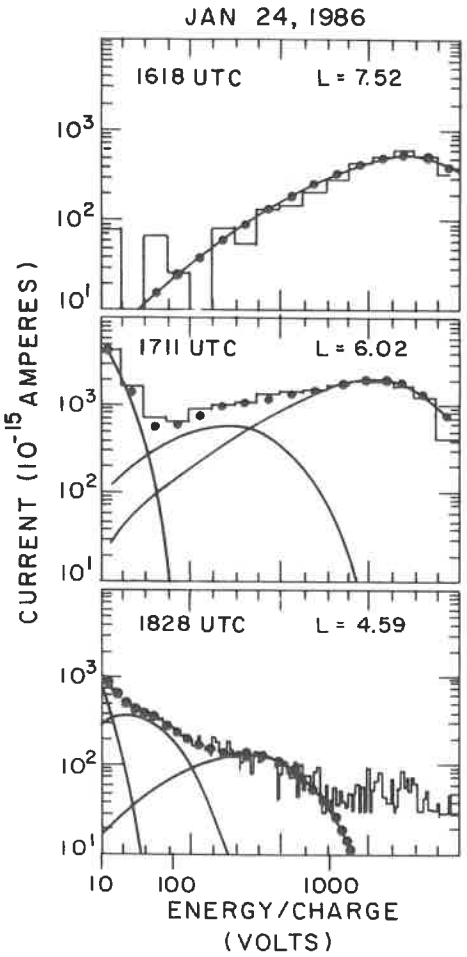

Fig. 6. Examples of positive-ion spectra in the *M*-mode, with least-squares fits to convected Maxwellians shown (figure after Selesnick and McNutt 1987). The vertical scale is current in femptoamperes and the horizontal scale is approximately logarithmic in energy-per-charge from 10 V to 5950 V. The histogram represents the observed currents, the solid curves are the currents due to the individual Maxwellian distributions, and the dots are the sum of the currents due to the Maxwellian distributions.

et al. 1986*a*). Thus, in the observations discussed below, the positive ions are assumed to be protons.

Morphology of the Electron and Positive-Ion Measurements

Color Plate 1 gives an overview of the morphology of the PLS data collected in the inner magnetosphere of Uranus, from 1500 to 2400 UTC on 24 January 1986, corresponding to a range of radial distances from Uranus

of 8.1 R_U inbound to 14.2 R_U outbound. The display is a color energy-time spectrogram showing both electron and positive-ion measurements (long integration time). The first and second panels from the top show, respectively, *E*2 electron spectra (140 V to 5950 V) and *E*1 electron spectra (10 V to 140 V). The third panel shows *L*-mode positive-ion spectra (10 V to 5950 V) acquired with the D cup or side sensor, and the fourth panel shows *L*-mode positive-ion spectra acquired with the C cup of the main sensor cluster. The color bar at the bottom of the Plate indicates the relative intensity of the particle fluxes displayed.

As noted above, the positive-ion spectra in the *L*-mode are acquired every 48 s, so for purposes of display in Plate 1, the electron spectra that are acquired half as often occupy twice the time interval of their ion counterparts. Similarly, every 12 min there is a gap in the collection of *L*, *E*1 and *E*2 spectra corresponding to the time interval in which the positive-ion *M*-mode data are accumulated; for display purposes, the *L*, *E*1 and *E*2 spectra just preceding this gap are repeated during the gap. The feature from 1621 to 1649 UTC in the *E*1 and *E*2 panels occurs during a roll maneuver when sunlight entered the D cup and produced a spurious signal in that sensor; this interval should be considered a data "gap" for the electron measurements. Throughout the encounter period, anomalously large fluxes were measured in the high energy-per-charge channels of the C cup (from ~1 kV to ~6 kV). These can be seen in the bottom panel of Plate 1 throughout the entire time period depicted. Signals of this type have been apparent since the encounter with Jupiter and are known to be an instrumental effect, possibly associated with radiation damage sustained by the instrument in the Jovian radiation environment.

The major morphological features shown in Plate 1 can be summarized as follows. The first indication of plasma was a rise in the hot ion fluxes in the upper energy channels for the *L*-mode D-cup spectra (LD panel in Plate 9) at about 1500 UTC, near $L \approx 9$ (all *L*-shell values quoted are based on the OTD model of Ness et al. 1986). The warm ions and the cold electrons appeared at 1648 UTC, near $L \approx 6.6$ as is evident in the lowest channels of the LD and *E*1 panels. Note that this time was near the crossing of the terminator (cf. Fig. 2), so that essentially all the electron and warm ion fluxes occurred on the night side of the planet. The shaded portions of the trajectory in Fig. 4 indicate regions where the hot and intermediate ion components were both simultaneously observed. The electrons (but not the ions) exhibited a drop and rapid recovery in flux just before the ring plane crossing (indicated by RP on Plate 1) at 1716 UTC, probably due to a cooling of the electron population to temperatures well below the instrument threshold of 10 V.

In one of the most dramatic features of the encounter, the hot and intermediate ion and electron fluxes near closest approach exhibited a precipitous "drop-out" and a subsequent recovery about 1 hr later, at the "plasma edges" at 1736 UTC ($L \approx 5.3$) and 1854 UTC ($L \approx 4.8$). The locations of these

plasma edges are indicated on all of the trajectory plots described above (Figs. 2, 3, 4). The warm ion fluxes were reasonably continuous across these edges. Inside the plasma edges (between 1736 and 1854 UTC), the warm ion fluxes fluctuated considerably, although their overall fluxes continued to increase, peaking just after closest approach (cf. panel LD in Plate 1). In this innermost region, the electron fluxes decreased to very low levels, again apparently because the electron temperatures dropped well below the 10 eV energy threshold of the PLS instrument.

The outbound plasma edge was characterized by a dramatic increase in the fluxes of hot electrons, with an intense flux of 2- to 4-keV electrons encountered in the outbound region. The energetic electron fluxes continued to be elevated for about 4 hours after the crossing of the outbound plasma edge at 1854 UTC. These fluxes were evidently responsible for the spacecraft acquiring a large negative potential outbound. This potential accelerated warm protons into the PLS detectors and produced the striking feature visible in the positive-ion spectra (LD and LC) between 1929 and 2152 UTC in Plate 1, with a concurrent disappearance of the low-energy ($E1$) electron fluxes. The apparent energy cutoffs in the $E2$ spectra in this period were due to instrumental effects in this environment. Features in the ion spectra indicate that the spacecraft potential reached -400 V during solar occulation. The hot electron fluxes persisted until 2250 UTC, where they suddenly dropped to background levels. The boundary at 2250 was also marked by large decreases in energetic particle fluxes (Krimigis et al. 1986*a*; Stone et al. 1986), and evidently defines the high latitude boundary of the plasma sheet at $L \approx 18$, above which the spacecraft entered open field lines (as discussed below).

Plasma Parameters in the Inner Magnetosphere

The spectra shown qualitatively in Plate 1 can be analyzed quantitatively to obtain plasma parameters describing the character of the electrons and positive ions in this region. Figure 7 is a display of the densities and temperatures of the warm, intermediate and hot proton components, as a function of L-shell and UTC on 24 January 1986 (after Selesnick and McNutt 1987). Figure 8 is a display of the cold electron densities and temperatures (n_c and T_c) and the hot electron densities and temperatures (n_h and T_h) as a function of UTC and L-shell (after Sittler et al. 1987). In discussing these plasma parameters, the inner magnetosphere is conveniently divided into 5 distinct regions.

Region I

This region extends from 1500 UTC to 1648 UTC ($L \approx 9$ inbound to $L \approx 6.6$ inbound). After the inbound magnetopause crossing at 1007 UTC (at 18 R_U), the first indications of plasma in the inner magnetosphere are low

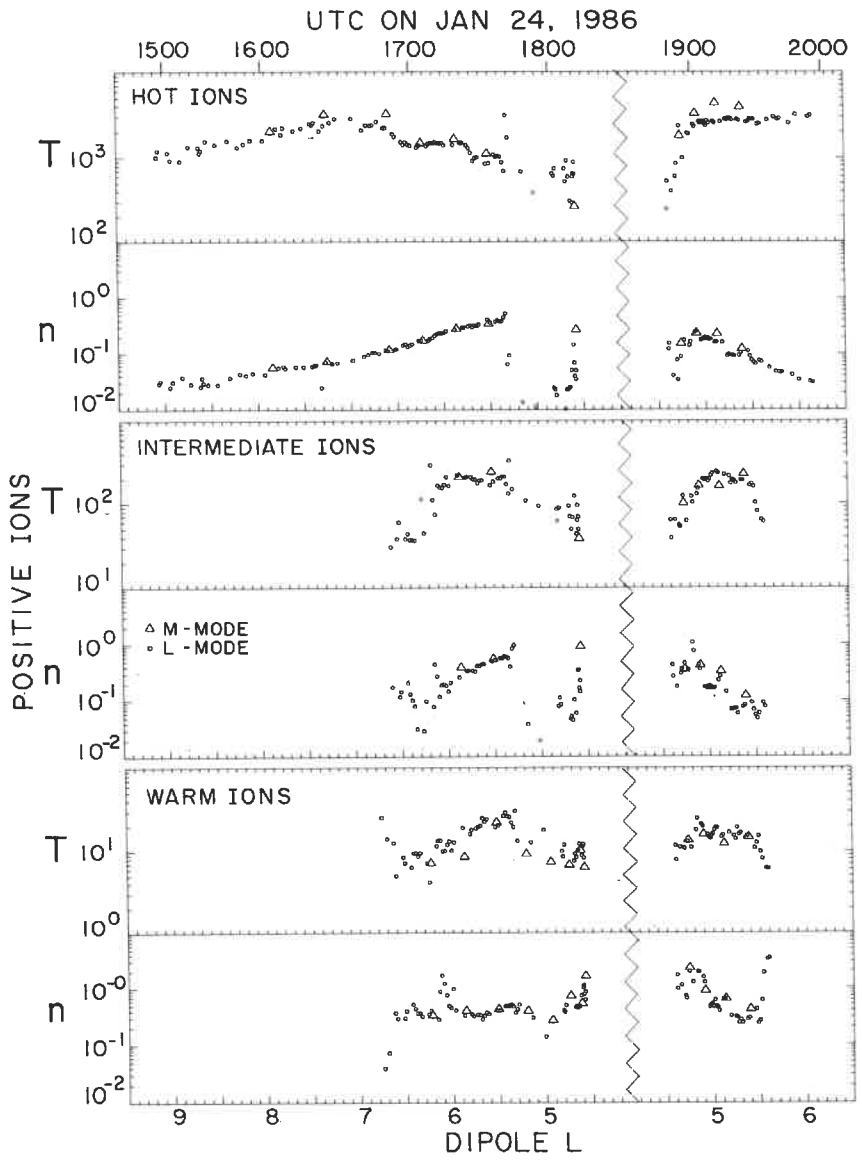

Fig. 7. Density (cm^{-3}) and temperature (eV) vs dipole L (bottom) and time (top) for each of the three Maxwellian components used in modeling the positive-ion data (figure after Selesnick and McNutt 1987). The large open triangles indicate values from M-mode spectra, and the small circles values from L-mode spectra.

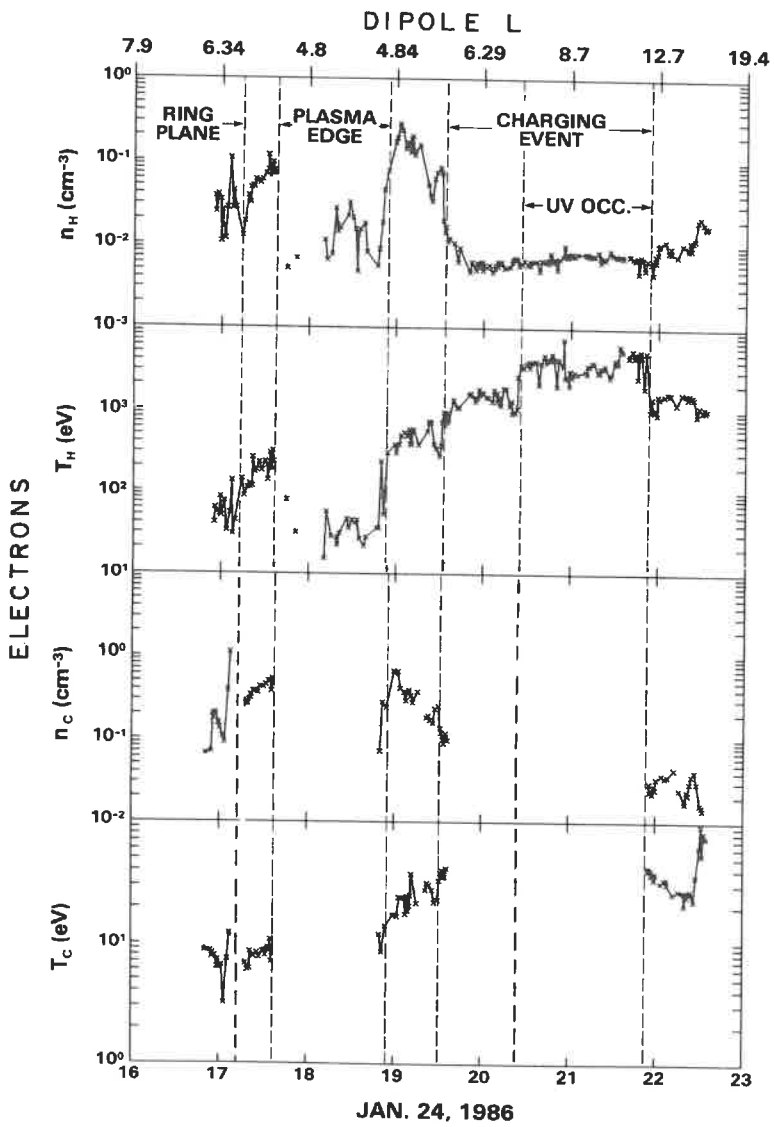

Fig. 8. Density and temperature of the cold electron (bottom panels) and hot (or halo) electron (top panels) components in the inner magnetosphere of Uranus (figure after Sittler et al. 1987). Near the ring plane and within the plasma edges and the spacecraft charging event, the cold electron component was not observable. At the top of the upper panel, we indicate the dipole L value of the Voyager 2 spacecraft.

fluxes of hot protons appearing about 1500 UTC ($L \approx 9$). In the region from 1500 to 1648 UTC ($L \approx 9$ to $L \approx 6.6$ inbound), only the hot proton component is present. The D cup L-mode spectrum taken in this region at 1618 UTC ($L = 7.52$) is shown in the top panel of Fig. 6 with the fit to the data superimposed. No electron currents above noise level were observed in this region (with the exception of the spurious signals associated with sunlight, as mentioned above).

Region II

This region extends from 1648 UTC to 1736 UTC ($L \approx 6.6$ inbound to $L \approx 5.3$ inbound). The warm ion component appeared suddenly at 1648 UTC ($L \approx 6.6$), increasing in density by a factor of 10 during the 96 s covered by 3 consecutive L-mode measurements (cf. the bottom panel of Fig. 7, which is a display of the density of the warm ions). This corresponds to a distance traveled by the spacecraft of about 2000 km. Electrons with a temperture T_e of 25 eV appeared simultaneously with the appearance of the warm ion component. The temperature T_e is derived from a moment integration over the entire electron distribution; the cold component temperature T_c at this point was 10 eV (cf. the bottom panel of Fig. 8). An example of an electron spectrum in this region (at 1731 UTC) is given in Fig. 5, left-most panel (with a Maxwellian fit to the cold electrons). A similar example of a positive-ion spectrum in this region (at 1711 UTC) is given in Fig. 6, middle panel (with fits to all 3 ion components). After 1648 UTC, all three Maxwellians referred to above are used in fitting the ion data. It appears that the hot and intermediate components are part of a smooth distribution at high energies (also evident in Plate 1), whereas the warm component is separate from the other 2 components. Both components of the electrons, and both the intermediate and hot ions, show a rise in density over Region II, up to the sharp drop at 1736 UTC ($L \approx 5.3$).

From 1709 UTC to 1715 UTC, just before the predicted ring plane crossing at 1716 UTC, there was a marked electron density reduction which was not observed in the ions (cf. Plate 1 and Figs 7 and 8). Sittler et al. (1987) interpreted this apparent density drop to a cooling of the electrons (to $T_c < 2$ eV), with the result that the thermal electron energy moved well below the PLS 10 V cut-off.

Region III

This region extends from 1736 UTC to 1854 UTC ($L \approx 5.3$ inbound to $L \approx 4.8$ outbound); it is bounded by the plasma edges at 1736 UTC and 1854 UTC. Although there was a precipitous drop in the hot electron, hot ion, and intermediate ion densities at the inbound plasma edge at 1736 UTC, the warm ion densities were reasonably constant across that plasma edge (cf. Fig. 7). The drop in the hot ion density actually occurred slightly earlier than for the intermediate ion density, by a distance corresponding to about 2 or 3 L-mode

measurements. This corresponds to a distance traveled by the spacecraft of about 2000 km. From Plate 1, it is apparent that the earlier disappearance of higher energies at the inbound plasma edge is characteristic of both higher-energy ions and higher-energy electrons. Inside the boundary the hot and intermediate ion components sometimes appear, but seem to form a high-energy tail on the warm component that is evident throughout the region. This suprathermal ion tail is seen most dramatically in the *M*-mode spectrum at 1828 UTC ($L = 4.59$) (see Plate 1 and the bottom panel of Fig. 6). The suprathermal component was not always present throughout the region. For example, the next *M* mode taken at 1840 UTC ($L = 4.62$) is well represented by a single warm component, with no suprathermal tail. Throughout this region, there was a large discrepancy between the ion and electron densities, which is again attributed to a cooling of the thermal electron population to well below the 10 V threshold of the PLS instrument, similar to the feature near the ring-plane crossing. Also, $T_h < 40$ eV here, with a strong attenuation of hot electron fluxes evident (see Plate 1 and Fig. 8). The outbound plasma edge crossing is less distinct in the positive-ion spectra than inbound. It started at about 1850 UTC, $L \approx 4.7$, again with lower energies closer to the boundary. This boundary is more clearly evident in the PLS electron data (see Plate 9).

Region IV

This region extends from 1854 UTC to 1929 UTC ($L \approx 4.8$ outbound to $L \approx 5.6$ outbound); it extends from the outbound plasma edge to the beginning of the charging region at 1929 UTC. Its dominant feature is the dramatic increase in the fluxes of hot electrons evident in Plate 1 and in the top panels of Fig. 8. The middle and rightmost panels of Fig. 5 show electron spectra from this region. Note that both the cold and hot electron temperatures were significantly higher in this outbound region compared to inbound. In this region, the positive-ion spectra again became relatively featureless, with the warm component just visible in the low-energy channels and an almost flat distribution at higher energies. The density of the hot ion component peaks at about 1900 UTC ($L \approx 4.8$), and thereafter the plasma density decreases rapidly.

Region V

This region extends from 1929 UTC to 2250 UTC ($L \approx 5.6$ outbound to $L \approx 18$ outbound); it includes the period of spacecraft charging (1929 UTC to 2152 UTC), as evidenced by the "beamlike" signature in the positive-ion mode (cf. Plate 1, particularly the LD panel). This beam is thought to be the warm ion component accelerated up to as much as 400 V by a negative spacecraft potential of this magnitude. The charging event is discussed at length in a separate section below, since its characteristics constitute strong

evidence for the absence of a population of cold ions "hidden" below the 10 V threshold of the PLS instrument.

At about 1940 UTC, the intermediate ion component ($T \sim 50$ to 100 eV) went below the noise level of the instrument in a fairly symmetric, but somewhat less distinct manner compared to its rise on the inbound leg of the spacecraft trajectory (see Fig. 7). The disappearance of the intermediate component outbound was not as clearly located as its appearance inbound, owing to the onset of the spacecraft charging event at about the same time. The inbound appearance was at $L \approx 6.2$ whereas the outbound disappearance was at $L \approx 5.7$. The change in L between the plasma edge boundary and the disappearance of the intermediate component was about 0.9 both inbound and outbound. The two regions where both the hot and intermediate components were detected are shown as the shaded regions along the trajectory in Fig. 4. The sudden apparent rise in density at the end of the warm component plot in Fig. 7 is spurious and caused by positive ions being accelerated into all 4 detectors by the negative spacecraft potential, indicating the start of the charging event (in the analysis of Fig. 7 the spacecraft potential was assumed to be zero).

The hot positive-ion component was not strongly affected by the charging event because the largest spacecraft potential was ~ -400 V compared to ~ 3 kV for the energy-per-charge of the hot component, and, as shown in Fig. 7, its density continued to decrease in the charging event. Throughout the charging event, the hot ion component exhibited low fluxes that followed the more intense signals observed by the PLS electron measurements at the same time (Sittler et al. 1987). This behavior can be seen in Plate 1. Between 2000 UTC and 2230 UTC the ion signals were sufficiently low to preclude accurate analysis. The density of the hot component in the region up to about 2230 UTC ($L \approx 15.5$) was typically on the order of 0.01 to 0.05 cm^{-3}. The fluxes of both electrons and positive ions dropped below the detection level of the instrument in the interval from 2230 to 2250 UTC, and remained close to that level (except for 4 traversals of the plasma sheet, discussed below) until the outbound magnetopause crossing at 0700 on January 26.

It is worth while pointing out that the moment calculation used to derive values for T_h in Fig 8 is truncated at the 6 keV cutoff of the instrument, and no attempt is made to extrapolate beyond this maximum energy. In the interval from 2025 UTC to 2150 UTC, there were probably significant electron fluxes above 6 keV (cf. Plate 1); the estimates of T_h in Fig. 8 should be considered lower limits.

The Spacecraft Charging Event

The charging of spacecraft to large negative potentials in the presence of hot electrons is a well-known phenomenon in the magnetosphere of the Earth (see, e.g., Garrett 1981, and references therein). The large outbound

fluxes of keV electrons apparently were responsible for driving the spacecraft potential negative with respect to the surrounding plasma. A positive-ion beam first appeared in the D cup around 1929 UTC; at this time intense electron fluxes began to move to higher and higher energies (see Plate 9), with the peak electron flux eventually moving above the high-energy cutoff of the instrument at 5950 V. The positive-ion beam vanished near 2152 UTC, although the high-energy electron fluxes persisted for almost another hour (see Plate 1).

Figure 9 displays a set of *M*-mode spectra from the charging region. The signature of accelerated positive ions, which is clearest in the data of the D cup, shows a peak with a sharp falloff at high energy and a more gradual decrease at lower energies. The location of the peak is a measure of the ion speed into the cup (which was highly supersonic), and the detailed nature of the high energy fall-off in signal indicates the temperature of the beam. The low-energy decrease is primarily determined by the details of the response function of the instrument. The presence of cold beams into all 4 cups simultaneously can only be explained by an electric field accelerating the ions into the cups; hence, the spacecraft must have charged to a negative potential with respect to the plasma. The cold electrons disappeared simultaneously with

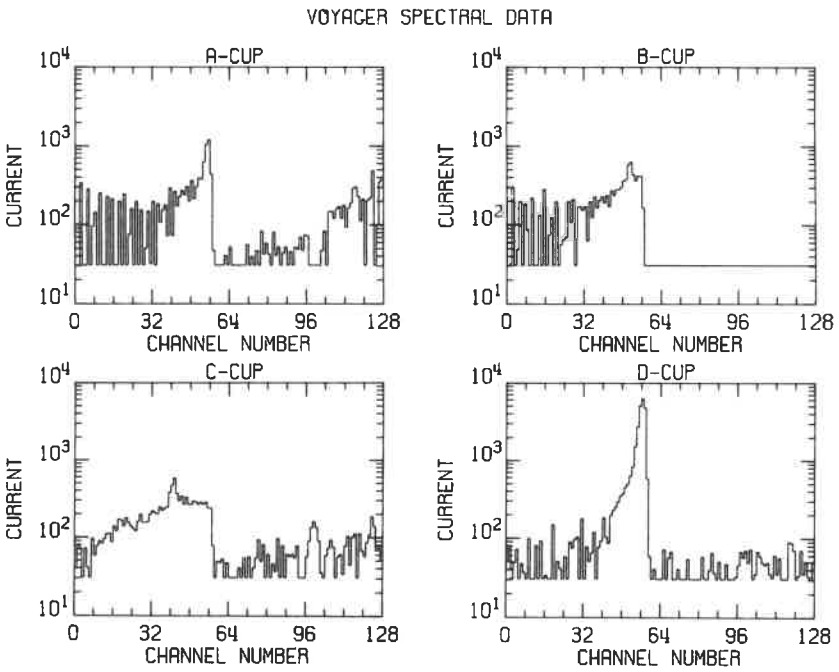

Fig. 9. *M*-mode spectrum for all 4 sensors acquired near 2040 UTC on 24 January 1986 (figure after McNutt et al. 1987). Current in femptoamperes is plotted vs linear channel number, which is approximately logarithmic in energy-per-charge from 10 V to 5950 V.

the appearance of the proton beam (cf. Plate 1), and this phenomena is also consistent with the negative charging hypothesis.

When the photoelectron flux from a spacecraft is dominated by the plasma electron current to the spacecraft, the spacecraft will charge negatively to a potential comparable to the mean energy of the electrons dominating the plasma electron current (i.e. $e\phi_{sc} \approx -kT_e$). When the spacecraft charges to a negative potential, plasma electrons experience a deceleration as they pass through the sheath surrounding it. If the temperature of the cold electrons is less than the magnitude of the charging potential, the cold electrons are unable to penetrate the potential barrier surrounding the spacecraft, and will not be detected. This phenomenon explains the dropout of the thermal electrons during this period (see Plate 1 and Sittler et al. 1987, Fig. 9). The lack of signal in the low-energy portion of *E*2 in this period (cf. Plate 1) is due to the production of secondary electrons within the instrument housing and details of the instrument operation.

McNutt et al. (1987) analyzed spectra such as in Fig. 9 and derived ion plasma parameters in this region. The magnitude of the spacecraft potential and the ambient proton densities obtained from this analysis are displayed in Fig. 10 for the period from 1939 UTC to 2158 UTC. Only the more reliable densities obtained from the *M*-mode spectra are shown in the bottom panel. Neither the densities nor the temperatures (not shown) exhibit systematic behavior with distance from the planet. However, the densities in *L* shells between 7 and 12 are larger than inbound values in the same *L* shells (cf. Fig. 7). The spacecraft potential exhibits systematic variations. As the flux of high-energy electrons increased, the potential changed from about -50 V (1940 UTC) to about -120 V. The potential changed discontinuously at the entry of the spacecraft into the shadow of the planet (nominal time 2024 UTC) and at the exit of the spacecraft from the shadow (nominal time 2144 UTC). These times are indicated in Fig. 10. The changes in potential that occurred at these times can be understood qualitatively as being caused by the shut off of production of photoelectrons from the spacecraft surfaces because of the disappearance of the solar ultraviolet. Normally, the photocurrent prevents large negative potentials from being reached in sunlight. Upon entering the shadow of the planet, this current source was turned off, and Voyager rapidly reached a new equilibrium potential that varied in the range of -300 to -400 V. Around 2053 UTC, the potential shifted discontinuously, decreasing in magnitude to about -180 V. This occurred while the spacecraft remained in Uranus's shadow, with no noticeable shift in the electron spectra at high energies (cf. Plate 1). The decrease in magnitude of the potential, which began upon exiting the shadow, occurred prior to the nominal time of occultation egress and was more gradual than the change in potential at entry into the planet's shadow. The last clear evidence of a negative potential on the spacecraft was in the *M*-mode spectrum at 2152 UTC, which indicates a potential of -28 V.

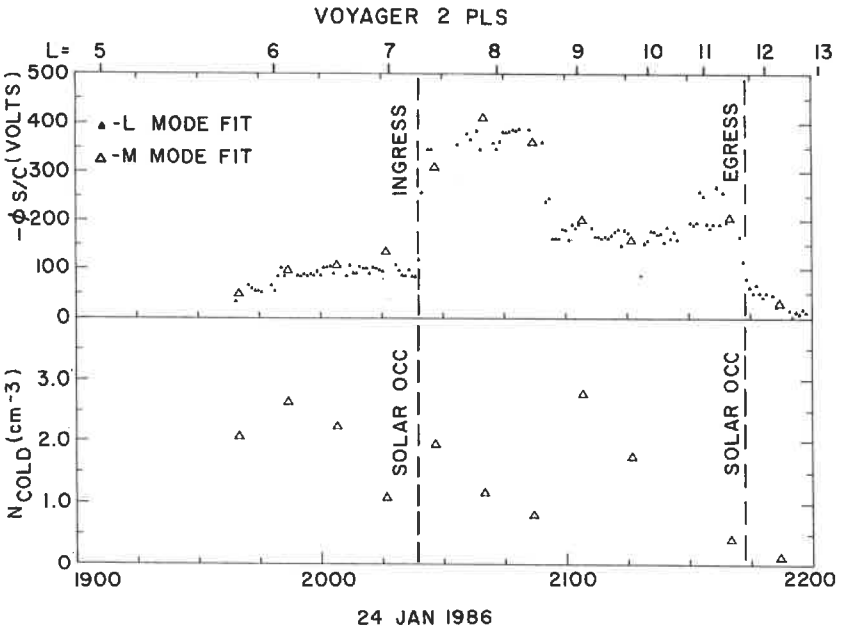

Fig. 10. Plasma densities and magnitude of the spacecraft potential in the charging region (after McNutt et al. 1987). Density estimates are possible only for the *M*-mode spectra. The magnitude of the spacecraft potential is estimated from the high-energy cutoffs in both the *L*-long and *M*-mode spectra. Nominal times at which Voyager 2 entered the shadow of Uranus (solar occulation ingress) and left the shadow (solar occulation egress) are also indicated. Note that the potential is negative.

The crucial point of this analysis is that the estimated temperatures from the region in which the spacecraft was charged negatively are comparable to those found inbound, not an order of magnitude lower (i.e., characteristic of a hidden cold population). If we assume that the thermal structure of the proton distribution functions was not radically different between the inbound and outbound measurements, the measurements made while the spacecraft was charged imply that there is no cold pick-up distribution below the 10 V threshold of the PLS experiment on the day side of the planet, because the large negative potential acquired by the spacecraft in this region was sufficient to accelerate all positive ions above the energy threshold of the PLS experiment, assuring their detection. The large potentials, inferred temperatures, and qualitative similarities between features in the spectra observed both inbound and outbound argue that the temperature of the thermal population is everywhere greater than a few electron volts and that all of the low-energy proton population within the magnetosphere of Uranus was detected by the PLS experiment. Estimates of electron density by the plasma wave (PWS) experiment (Kurth et al. 1987) are consistent with the PLS determinations

throughout the inner magnetosphere, also indicating that a hidden component is not present.

Flux Tube Content η and the Energy Invariant λ

In discussing the significance of these observations in the subsequent sections, it is useful to derive two additional parameters from the data sets presented above, following Selesnick and McNutt (1987). The first of these is the number of particles per unit magnetic flux, or flux tube content, as given by

$$\eta = \int \frac{n\, ds}{B} \tag{1}$$

where n is the local number density, B is the magnetic field magnitude, ds is an element of arc length along a magnetic field line and the integral extends along the entire length of the field line external to the ionosphere. A population of particles with common values of the first two adiabatic invariants, μ and J, moving under the influence of electric field and magnetic gradient and curvature drifts on an equipotential field line, conserves its flux-tube content along each drift trajectory (Roederer 1970). In a region of space without significant sources or losses, supplied by plasma from a uniform external source, the total flux-tube content given by Eq. (1) should be uniform except where a given particle population is excluded by its drift trajectories. The number density is assumed to be constant along a field line, which should be true for an isotropic distribution function, as discussed earlier. The flux-tube content is then equal to n times the flux-tube volume per unit magnetic flux, which for a dipole field gives $\eta \approx n\mathrm{R_U}\mathrm{L}^4/B_o$ where $B_o\mathrm{R_U}^3$ is the magnetic dipole moment of Uranus.

Adiabatic compression of an isotropic, monatomic gas also conserves the quantity $KV^{2/3}$ where K is the average energy and V is an effective volume, i.e., the flux-tube volume per unit magnetic flux ($\mathrm{R_U}L^4/B_o$ for a dipole field). The relevant energy invariant is therefore $\lambda = KL^{8/3}$ to within an arbitrary constant. For future reference, note that the density should vary as L^{-4} for constant flux tube content, and that the average energy should vary as $L^{-8/3}$ for constant energy invariant. For most of the time, the hot and intermediate ion components seem to be part of a single non-Maxwellian distribution, and η and λ have been computed using the sum of the two densities, the average energy weighted by the densities and the OTD magnetic field model. They have also been computed for the warm component separately. These are shown vs dipole L in Fig. 11. Also shown are the corresponding plots for the fits to the PLS electron measurements by Sittler et al. (1987).

From Fig. 11 it is seen that η and λ are both approximately constant along the inbound leg of the spacecraft trajectory from $L \approx 9$ to $L \approx 7$, al-

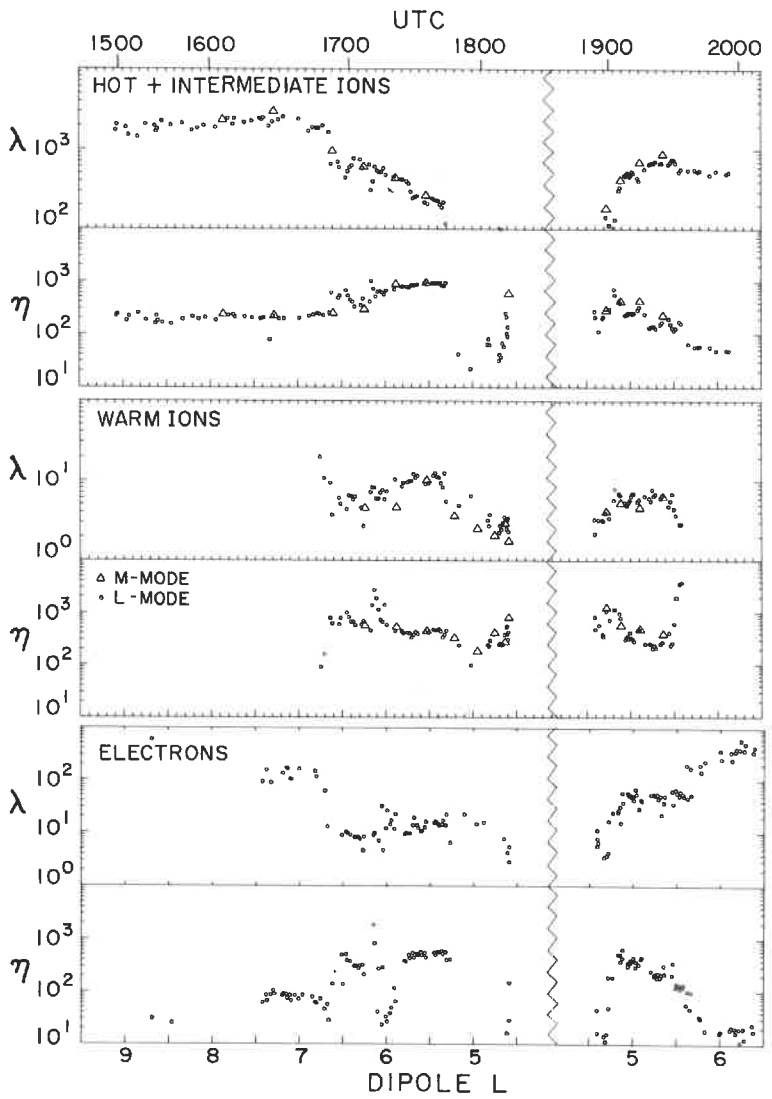

Fig. 11. Flux-tube content η, and energy invariant λ, vs dipole L, for the combined hot and intermediate Maxwellian ion components in the top panel, the warm ion component in the middle panel, and the total observed electron population in the bottom panel (figure after Selesnick and McNutt 1987). The quantity η has units of particles cm^2 G^{-1} and the units of λ are arbitrary.

though the spacecraft was almost certainly not moving along a flux-tube drift trajectory. At $L \approx 7$, the flux-tube content began to increase, as shown in Fig. 11, and the average energy and energy invariant began to decrease. The increase in flux-tube content began with the hot component but shifted to the intermediate component soon after it appeared. The total flux-tube content of the hot and intermediate components increased by a factor of about 5 between $L \approx 7$ and the sharp drop at $L = 5.3$. The energy invariant decreased by a factor of about 10 in the same interval. After the reappearance of the hot and intermediate components at $L \approx 4.8$ outbound, the variation in η and λ with L was similar to that along the inbound leg. Problems with the data analysis in this region, as described by Selesnick and McNutt (1987), may mask some of the trends. The electron flux-tube content shows a trend similar to that of the high-energy ions, indicating that *all* of the detected electrons seen were probably associated with these ions.

Dispersive and Nondispersive Events

The most prominent feature in Plate 1 is the sharp dropout at the plasma edges across most of the PLS energy range at about 1736 UTC, followed by an almost equally sharp rise in density at about 1854 UTC. However, the most gradual feature preceding the drop-out is equally distinctive. This feature starts at about 1620 UTC when the ion distribution function begins to spread from high-energy channels to fill in all of the lower energies; the electrons then appear at low energies and begin to fill in the higher energies until the sharp drop-out is reached. The rise and fall in flux-tube content are called "dispersive" if various energy components appear well separated in time and "nondispersive" if they appear essentially simultaneously. Using this terminology, the inbound plasma edge showed slight energy dispersion, with the highest energies dropping about 2 min (corresponding to a distance of about 2000 km) before the lowest, but the event was basically nondispersive. In contrast, the more gradual structure preceding it was clearly a dispersive event.

For a plasma that is drifting while conserving the first 2 adiabatic invariants, or one that maintains an isotropic distribution through the effects of strong pitch angle scattering, the number of particles in a flux tube of unit magnetic flux should be conserved in the absence of any plasma sources or sinks (see e.g, Wolf 1983). Therefore the plasma density and the temperature should vary with magnetic field intensity in a predictable way if there are no gains or losses. These conditions were satisfied by the hot (~1 keV) ion component in the region outside $L \approx 6.6$ (1648 UTC) on the inbound portion of the trajectory, but they began to be violated when the distribution started to fill in at low energies (cf. Fig. 11). When the plasma edge was reached at 1740 UTC ($L \approx 5.3$), the flux-tube content had increased by roughly a factor of 5, at which point it dropped by over an order of magnitude. The dispersive rise in flux-tube content was gradual and occurred earlier for higher energies,

whereas the drop was sudden (nondispersive) and occurred almost simultaneously for all energies. The electron component showed a structure in flux-tube content similar to that of the hot ion component while the warm (~10 eV) ion component did not follow as distinctive a pattern. Although the data were not as clear or as extensive, on the outbound leg of the trajectory the flux-tube content varied with L in a manner similar to that on the inbound leg, starting with the sharp rise at about 1850 UTC ($L \approx 4.8$).

III. THEORETICAL INTERPRETATION OF OBSERVATIONS IN THE INNER MAGNETOSPHERE

Co-rotational and Convective Flows at Uranus

The major surprise of these plasma observations was the large day-night asymmetries seen deep in the inner magnetosphere. According to pre-encounter expectations, this inner region should lie deep inside a co-rotating Uranian plasmasphere, with little day-night structure. This was certainly not the case, as is seen most dramatically in the high electron fluxes outbound as contrasted to the low levels inbound. This difference must be a day-night effect, and not a magnetic latitude effect associated with pitch angle anisotropy, most obviously because there was a magnetic latitude crossover near $L = 8$ (cf. Fig. 3). If the inbound-outbound asymmetries were due mainly to the differing magnetic latitudes of the spacecraft, the fluxes at the crossover should have been the same inbound and outbound, and in fact they were dramatically different (Plate 1). The plasma densities in Figs. 7 and 10 also support a day-night structure. The densities were higher on the night side of the planet as compared to the day side for a given L-shell. In addition, significant electron fluxes and warm ion fluxes were not observed until 1648 UTC on the inbound pass (L ~6.7 inbound), but no such boundary was observed at 2012 UTC on the outbound pass (L ~6.7 outbound); this suggests that the boundary at 1648 UTC was a boundary in local time and not in radial distance. These are not signatures one would expect deep within a subsonic plasmasphere shielded from the day-night asymmetries associated with solar-wind-driven convection.

Shortly after the Uranus encounter, these observations led to a reconsideration of the manner in which plasmaspheres form. The formation of the plasmasphere at the Earth (Nishida 1966) is the result of the superposition of the electric field due to the rotation of the Earth and the solar-wind-induced convection electric field of the type proposed by Axford and Hines (1961) and Dungey (1961). Planetary rotation dominates in the high-density plasmasphere where plasma streamlines circle Earth and residence times are long. Outside this region, the convection electric field imposed by the solar wind dominates and low-energy plasma is rapidly convected sunwards and removed from the magnetosphere, leading to low densities in the convection-

dominated region. Brice and Ioannidis (1970) applied this formalism to Jupiter and found that the plasmapause there would extend all the way to the dayside magnetopause. As a result, most of the magnetosphere of Jupiter is plasmaspheric in nature, rotating with the planet and exhibiting high densities owing to the long residence time of the plasma. Siscoe (1978*a*) scaled the plasmapause location from the Earth to the other planets and concluded that all the large outer planets should have similar magnetospheres.

Upon reflection, it was realized that this classical analysis does not apply at Uranus. Solar-wind-driven convection and planet-driven co-rotation are in fact *decoupled* at Uranus (Vasyliunas 1986; Selesnick and Richardson 1986; Hill 1986). This decoupling arises basically because the solar-wind-driven convection at Uranus is perpendicular to the plane of co-rotational flow, instead of within that plane, as at the other planets. Consequently, convection penetrates deep into the inner Uranian magnetosphere, sweeping out the magnetospheric plasma on relatively short time scales and preventing the formation of a dense plasmasphere.

Selesnick and Richardson (1986) considered the formation of plasmaspheres for arbitrary orientations of the planetary spin axis with respect to the solar wind flow direction, and of the magnetic dipole axis with respect to the spin axis. A traditional plasmasphere with particles on closed trajectories can occur only if the rotation and dipole axes are aligned. If they are not aligned, and the rotation axis is almost aligned with the solar wind flow direction, as at Uranus, no plasmapause boundary exists and solar-wind-driven convection is effective throughout the magnetsophere. Transport throughout the magnetosphere of Uranus is relatively rapid compared to that at Jupiter and Saturn, where the relative orientation between solar wind flow, the magnetic dipole direction, and the rotation axis is Earth-like and convection driven by the solar wind does not penetrate deep into the magnetosphere. At Uranus, in contrast, convection can penetrate deep into the inner magnetosphere, providing a natural explanation for the day-night asymmetries, and an important loss process for the plasma.

Plasma Transport Rates and Residence Times

Assuming that transport is due to convection, the residence time for plasma in the Uranian magnetosphere can be estimated, following the arguments of McNutt et al. (1987). A transport rate and the observed densities then lead to a source strength and possible sources for the observed plasma (see the next section). One of the determining factors for the transport rate is the coupling efficiency ξ of the solar wind to the magnetosphere, which determines the strength of the convection electric field. At Earth the coupling efficiency is about 0.2 when the direction of the interplanetary magnetic field allows reconnection to occur and about 0.04 if the interaction is via viscous processes. Dessler (1986) estimated the coupling efficiency at Uranus in the range $0.007 \leq \xi \leq 0.10$, based on energy arguments (see also McNutt et al.

1987). Given this coupling efficiency, we can estimate the convection time as the time required to cycle the flux in the magnetotail under the electromotive force provided by the solar wind (Siscoe 1975).

The maximum available convective *emf* is given by $\phi_c = 2 R_M V_{SW} B_{SW}$, where R_M is the radius of the magnetosphere ($R_M \sim 42$ R_U, the approximate tail radius [Ness et al. 1986]), V_{SW} is the solar wind speed ($\sim$400 km s^{-1}), and B_{SW} is the solar wind magnetic field strength ($\sim$0.1 nT). These values give $\phi_c = 92$ kV. The field strength measured in the magnetotail at the first magnetopause crossing outbound is 1.5 nT (Ness et al. 1986), so the flux in the tail, $\Phi_{tail} = \frac{1}{2} \pi R_M^2 B_{tail}$ (Siscoe 1975,1978*a*), is $\sim 2.7 \times 10^{-9}$ weber. The convection time T_c is then $\Phi_{tail} / (\xi \phi_c)$ where ξ is the coupling efficiency. Again using the quantities measured during the encounter, we obtain $T_c = 0.34/\xi$ days. Coupling efficiencies of 0.007 to 0.1 imply convection times of 48 to 3.4 days, respectively. We also note that the maximum (constant) convection electric field is 4.3×10^{-5} V m^{-1}, or about 1 kV R_U^{-1}. This corresponds to a (maximum) convection speed of $\sim$1.8 km s^{-1} at $L = 10$ (using the OTD model), which is small compared to the rigid co-rotation speed, as noted previously.

Other arguments give limits on the transport time that are consistent with and improve upon this range of values. Magnetospheric ions and electrons move under the influence of convection electric fields and also of gradient B drift in opposite directions around the planet. Gradient drift speeds can easily be calculated, and Sittler et al. (1987) used these calculations to estimate a range of convection time scales that are consistent with the symmetry or lack of symmetry of particle fluxes in local time and/or magnetic longitude. In the LECP energy range, the 20 keV electrons are clearly trapped, at least inside of $L = 9$; Mauk et al. (1987, Fig. 7) shows the latitude variations expected for a trapped distribution. The lack of strong asymmetries in the electron fluxes above 20 keV implies that the gradient drift speed for these particles is much faster than the convection drift speed; otherwise, azimuthal symmetry could not be attained. This constraint implies that convection times are $\gtrsim$1 day (cf. Sittler et al. 1987, Fig. 9, and related discussion). Conversely, the strong asymmetry observed in the hot electrons below 6 keV implies that the gradient drift speed for these particles must be much slower than the convection drift speed (neglecting losses), otherwise these particles would be azimuthally symmetric. This constraint implies that convection times are <3 to 10 days, depending on the convective electric field model. Given these bounds, and the bounds previously derived, it is henceforth assumed that the convection time scale at Uranus is of the order of 3 days. The actual range probably varies from 1 to 10 days, but all of our conclusions below remain qualitatively unchanged over this range.

As mentioned above, sputtering of water ice from the surfaces of the Uranian moons by high-energy particles should produce heavy ions in the magnetosphere (Cheng 1984). The absence of such ions indicates that transport must remove them before they reach measurable densities. Eviatar and Richardson (1986) modeled the plasma tori expected for each of the Uranian moons assuming such a sputtering source and negligible transport. This model is easily adapted to include convective transport and the observed fluxes of energetic particles. A residence time on the order of 3 days implies that heavy ion densities would never reach a level detectable by the PLS instrument (McNutt et al. 1987). Cheng (1987) has also shown that the unexpectedly large tilt of the magnetic field reduces the predicted fluxes of the water-group ions from previous estimates, so with hindsight, the lack of detection of heavy ions is not surprising.

The source of the warm proton component of the plasma is thought to be either the planetary ionosphere or the neutral hydrogen corona surrounding Uranus (Broadfoot et al. 1986), whereas the hot proton component is thought to be convected in from the magnetotail, with probably an ionospheric source. Plasma sources and source strengths are discussed at length in Sec. IV, but first a discussion of detailed transport of plasma within the magnetosphere is appropriate.

The Alfvén Layer Model

Given the theoretical conclusion that solar-wind-driven convection penetrates deep within the inner magnetosphere, the obvious question is whether the observed plasma features in the inner magnetosphere are consistent with such sunward convective flow. Within the model of convective plasma transport, there are several possible explanations for the density and energy structure observed. Quasi-steady phenomena are considered first. The sharp inner edge observed at $L \approx 5.3$ inbound and $L \approx 4.8$ outbound suggests that the plasma trajectories are excluded from the planetward region. Such a "forbidden zone" is characteristic of particles drifting under a general dawn-dusk convection electric field combined with the azimuthal magnetic gradient and curvature drifts of particles with significant thermal energy (see, e.g., Chen 1970; Roederer 1970). The boundary of such a zone is often called an Alfvén layer. Such zones have been studied in the context of the Earth's magnetosphere, but a simplification that is valid for Uranus is that the co-rotation electric field does not have to be included due to the orientation of the planetary rotation axis. At Earth the co-rotation electric field generates an azimuthal drift opposed to the magnetic drifts of the ions and in the same sense as those of the electrons. As a result, the ion drifts are more complicated and include the possibility of an extra forbidden zone not enclosing the planet. At Uranus such complications do not exist and the drifts of both ions and electrons are qualitatively similar to those of electrons at Earth, with the ion drift paths reflected across the noon- midnight meridian.

Based on the above estimates of the maximum convection electric field of about 1 kV R_U^{-1}, the Alfvén layers for some of the particles in the PLS energy range should be near $L = 5$. The problem is that the magnetic drift

speed is proportional to particle energy, and therefore the forbidden zones are larger for higher energies. In a dipole magnetic field with a constant convection electric field, the radius of the Alfvén layer would be proportional to the observed particle energy. Thus, if the inner edges observed near $L = 5$ represented Alfvén layers in an approximately uniform convection electric field, then significant energy dispersion should have been observed. As discussed above, only a very small energy dispersion was observed at the inner edges.

McNutt et al. (1987) and Selesnick and McNutt (1987) argued that the expected energy dispersion can be reduced by the inclusion of strong low-latitude shielding of the convection electric field at the inner edge. Gradient drifts of the high-energy particles in hot plasma drifting in from the tail lead to charge separation and the establishment of a partial ring current. The shielding of the convection electric field is caused by the opposite directions of the magnetic gradient drifts for ions and electrons, leading to a polarization electric field that partially cancels the convection electric field. This polarization electric field is reduced by Birkeland (field-aligned) currents that flow into the ionosphere.

The magnitude of these field-aligned currents is determined by an effective Hall conductivity $\Sigma_* \equiv \eta ec$ (Vasyliunas 1972) where η is the flux-tube content. Continuity of current in the ionosphere implies that the convection electric field is substantially modified if Σ_* is large compared to the ionospheric Pedersen conductivity Σ_P. With a substantially reduced convection electric field inside the edge, particles that drift into this region will be dominated in their subsequent motion by magnetic drifts which are azimuthal, so that further inward penetration will be suppressed. As more particles take part in the shielding process, it will gradually increase until a steady state is reached, leading to the formation of a sharp boundary. The electric field inside the ring-current region is then reduced by a factor on the order of Σ_P / Σ_*. Such shielding has been documented in numerical models of magnetospheric convection (see review by Wolf 1983) and in empirical models of the Earth's convection electric field (Volland 1973; McIlwain 1986).

The final quasi-steady location of the boundary adjusts itself so that the Birkeland currents flowing into the ionosphere are just balanced by ionospheric Pedersen currents. The latter are driven across the boundary by the polar cap potential. The location of the boundary is given approximately by

$$L_b = L_a \left[\frac{e\phi}{K_a} \frac{\Sigma_P}{\Sigma_*} + 1 \right]^{-1/3} \tag{2}$$

(Jaggi and Wolf 1973; Southwood 1977; Siscoe 1982). Here L_b is the L-value of the boundary, L_a the value at which the return Birkeland currents flow to the magnetopause, ϕ the potential drop across the polar cap, Σ_P the ionospheric Pedersen conductivity, and K_a the average particle energy at L_a. If we assume adiabatic compression, K_a is related to the average energy at L_b by

$$K_a = K_b (L_b/L_a)^{8/3}. \tag{3}$$

With typical values at Uranus of $L_b = 5$ at the boundary edge, $L_a = 20$ (radius of the magnetosphere), $K_b = 1$ keV (the hot proton population observed at the boundary), and $\phi = 20$ kV (see the above discussion), McNutt et al. (1987) found $\Sigma_p / \Sigma_* \sim 0.1$, consistent with the requirements for strong shielding of the convection electric field. This analysis also implies a "seed" population for the hot component with a temperature increasing from ~25 eV at $L = 20$. This population is not observed; however, assuming constant flux-tube content, the densities would be too low ($\sim 8 \times 10^{-4}$ cm^{-3} at $L = 20$) to have been detected with the PLS instrument.

Selesnick and McNutt (1987) modeled the above effects of the hot plasma on the convection electric field in more detail; Selesnick (1988) extended their calculations to include more realistic field models. Figure 12 shows equipotentials of the convection electric field calculated by these authors, using the same coordinate system as Fig. 4. The polar cap is taken to be at $L = 20$, and there is a constant electric field at higher L values in the

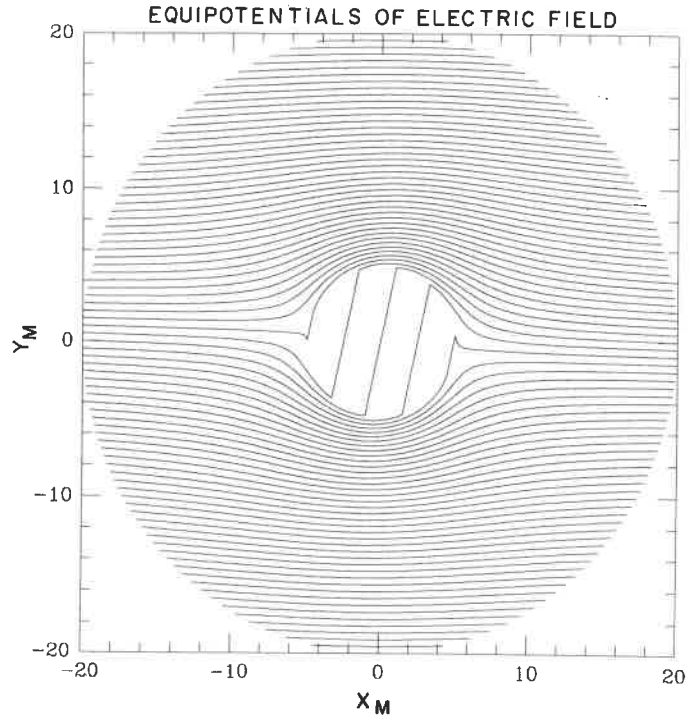

Fig. 12. Equipotentials of the model convection electric field described in the text. The equipotentials are calculated assuming a constant flux tube content outside of $L = 5$. The coordinate system is the same as that used in Fig. 4.

cross-tail direction (along the positive $\mathbf{Y}_M$ axis). To approximate the spatial distribution of the hot plasma, the flux-tube content is assumed to be constant for $L > 5$ and zero for $L < 5$ (Vasyliunas 1972). As described in the previous section, some energy dispersion is observed at the boundary; the lower-energy particles reach somewhat more planetward than those with high energies. This would be expected in a true, self-consistent determination of the plasma distribution. As shown in Fig. 12, some of the equipotential streamlines do penetrate the boundary. Low-energy plasma, for which magnetic drifts can be neglected everywhere, should drift along these streamlines with constant flux-tube content and thus penetrate the boundary.

Selesnick and McNutt (1987) also pointed out that, observationally, the plasma edge is a boundary for particles extending in energy from ~50 eV to ~5 keV. Since the gradient and curvature drifts are proportional to the particle energy and the magnetic field should be approximately constant across the boundary, the electric field must be shielded inside the boundary by about the ratio of the energy extremes of the boundary, or about a factor of 100. This dramatic shielding and the implied value of Σ_p / Σ_* is higher than the factor of about 10 derived by McNutt et al. (1987) from the above arguments based on Eq. (2), evidently due to uncertainties in the various parameters that were used in that argument. Just outside the boundary, Selesnick and McNutt (1987) found $\eta \approx 9 \times 10^{12}$ G^{-1} cm^{-2} (cf. Fig. 11), which leads to $\eta ec \approx 140$ mho (if only the hot component is used, η is somewhat smaller). A shielding ratio of 10 to 100 then implies 1.4 mho $\leq \Sigma_p \leq$ 14 mho in the ionosphere.

Atreya (1984) estimated that $\Sigma_P \approx 0.5$ mho for the ionosphere near the terminator; in auroral regions, the estimate for Σ_P was 5 to 10 mho for a power input of 10^{11} W from precipitating keV electrons (this is close to the 4×10^{10} derived from the Voyager 2 UVS observations). Thus the 1.4. to 14 mho range for Σ_P brackets estimates of conductance in the auroral regions. Mauk et al. (1987) have pointed out that such shielding calculations must include pressure due to particles in the energy range >28 keV, because that pressure is comparable to and sometimes greatly exceeds pressure due to particles in the PLS energy range (i.e. < 6 keV). However, the pressure gradient, and not the pressure, is the relevant physical quantity in these calculations: as the Low Energy Charged Particle Experiment (LECP) saw no structure similar to the plasma edges, the pressure gradient for particles in the LECP energy range is probably significantly smaller than that for particles in the PLS energy range. However, a close comparison of the gradients in PLS and LECP pressures has not yet been made.

Although the shielding appears plausible, we note that the Alfvén layer model requires a quasi-steady situation. In other words, time variations in the externally applied convection electric field should be slow enough that the Alfvén layer has time to adjust to different positions. Jaggi and Wolf (1973) and Southwood (1977) estimated the time τ_{shield} for shielding to be achieved after a sudden change in magnetospheric convection. This time scales as the size of the planet times Σ_P divided by the pressure of the magnetospheric plasma. Sittler et al. (1987) estimate τ_{shield} to be on the order of 2 to 20 hr at Uranus, with the uncertainty associated with the lack of knowledge of Σ_P. The time scale for variations in the convection electric field may be set by the rotation of the planet with a period of 17.24 hr (Desch et al. 1986) because the planetary magnetic field changes its orientation with respect to the interplanetary magnetic field due to the rotation. Therefore it is not clear whether the shielding time is short enough to maintain strong shielding and a thin boundary thickness in an Alfvén layer model for the plasma edges.

In the Alfvén layer model, all of the plasma outside of the convection boundary should be on trajectories of external origin (cf. Fig. 12). The flux-tube content should be conserved along these trajectories and hence everywhere outside of the boundary, if the external source is uniform and constant in time. As discussed previously, this is not true within about one L of the boundary, where η increases planetward. The increase in η may be due to a source of plasma within this region. A local source would have to produce plasma at the high energies, on the order of hundreds of eV to 1 keV, at which the gradient in η is observed. There is no obvious mechanism for producing plasma at such high energies, as discussed in the next section. It seems more likely that the high energies are produced by adiabatic compression and that the increase in η is caused by another mechanism.

Sittler et al. (1987) and McNutt et al. (1987) suggested that the explanation is a time dependent injection of plasma from the magnetotail caused by a substorm-type process similar to those in the Earth's magnetosphere, and that such a process could explain the dispersive energy dependence near $L = 6$ to 7 inbound, evident during the rise in η (as discussed further below). Mauk et al. (1987) and Cheng et al. (1987*b*) also concluded that substorm-like signatures occur in the energetic particle data at Uranus. The Alfvén layer model cannot easily explain the dispersive features because it would predict that outside the Alfvén layer the flux-tube content should be roughly uniform. It may be that a nonuniform source is supplying the flux-tube trajectories near the Alfvén layer with a higher flux-tube content, but it seems too coincidental to expect that the trajectories which reach closest to the Alfvén layer should come from the region with the strongest source. However, we cannot rule out this possibility.

The Injection Boundary Model

An alternative to the Alfvén layer model is the injection boundary model, originally suggested for Uranus by Sittler et al. (1987). At Earth, this model specifically requires strong time variations to explain dispersive features seen in the terrestrial magnetosphere (McIlwain 1974; Mauk and Meng

1983). In the injection boundary model, particles spanning a wide energy range are thought simultaneously to fill in the region tailward of a boundary on the night side of the Earth due to impulsive changes in the magnetospheric configuration during a substorm. Following injection, the particles drift under the combined action of a reduced convection electric field and magnetic drifts. Therefore, depending on the location of the spacecraft relative to the initial injection boundary at the time of observation, different energy dispersions can be seen.

Figure 13 shows a sketch from Sittler et al. (1987) (modeled after that of Deforest and McIlwain 1971), that may explain the structure in the initial inbound Voyager 2 dispersive event centered on 1648 UTC. The later arrival of higher-energy electrons compared to the higher-energy ions in this event is due to the fact that at this time the spacecraft is on the "dusk" side of the planet (cf. Fig. 4), where the counterclockwise drift of the ions from the tail is toward the spacecraft, whereas the clockwise drift of the electrons from the

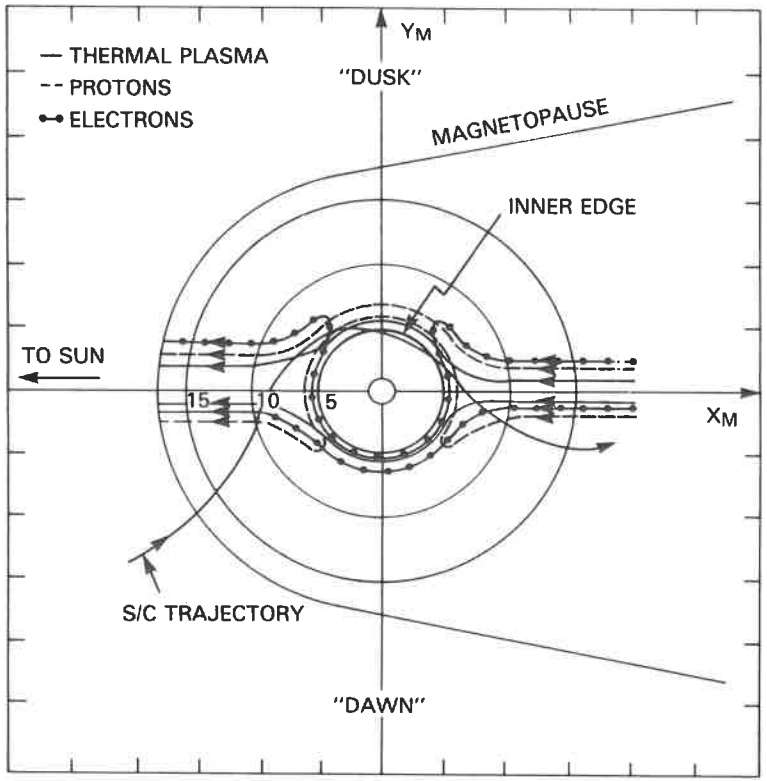

Fig. 13. Sketch of the different types of orbits for protons and electrons as they are injected from the magnetotail into the inner magnetosphere of Uranus (figure after Sittler et al. 1987). The coordinate system is the same as that of Fig. 4.

tail is away from the spacecraft. The initial spreading of the ion spectrum to lower energies near 1500 UTC is consistent with gradient drift since the higher-energy ions drift more rapidly around the planet, with their orbits confined to larger radial distances. In contrast, lower-energy electrons arrive earlier than higher-energy electrons, and simultaneously with lower-energy ions, because thermal ions and electrons are unaffected by gradient B drift and move along equipotentials of the convection electric field. Thus the observed energy disperion in this event is in good accord with that predicted by a time-dependent injection boundary model.

However, if the injection boundary model has some success in explaining the dispersive features, it has trouble with the nondispersive ones (i.e., the plasma edges). These cannot be explained by postulating that the injection took place with the spacecraft nearby before gradient drifts had time to separate the particles with different energies, because the inbound dispersive feature was seen before the nondispersive one and was associated with the same plasma cloud. There is no obvious way in the injection boundary model to explain the outbound features. These appear to be almost symmetric in L with those inbound, suggesting that they were part of the same structure seen at a later time and different magnetic longitude. This is more compatible with the Alfvén layer model in which the same layer could be crossed twice to give the two nondispersive signatures.

From the above discussion, it is evident that the Alfvén layer model is more suited to the two inner, nondispersive features in the data, while the injection boundary model has more success with the dispersive events. The situation is not surprising because the issue of which model is more applicable in interpreting satellite plasma data from the Earth's magnetosphere, especially from geosynchronous orbit, is a matter of some debate (Mauk and Meng 1983). Although a mechanism for producing the injection boundary is not clearly understood, the debate seems to be centered on the extent to which substorm-associated induction electric fields are important in influencing the dynamics of the inner magnetosphere. The injection boundary model requires that the impulsive propagation of a plasma front associated with such electric fields be the dominant mechanism for populating the regions near geosynchronous orbit, whereas the Alfvén layer model depends on these effects being small compared to the continuous influence of the convection electric field. Even if one of these is the dominant mechanism at Earth, the situation may be different at Uranus owing to the different configuration and extent of the magnetosphere.

Injection and Evolution in a Self-Consistent Electric Field

Selesnick (1988) suggested that both the dispersive and nondispersive features of the inbound event can be explained as plasma injection followed by the evolution of the injected plasma in a self-consistent electric field. He followed the evolution of a circular plasma cloud injected into the post-

midnight sector. The results 4 hr after injection are shown in Fig. 14, where the coordinate system is the same as in Figs. 4, 12 and 13. Here the initial boundary consists of both proton (indicated by + signs) and electron (indicated by − signs) components. The self-consistent field of both components is included. The protons have clearly drifted ahead of the electrons due to the opposite directions of their gradient and curvature drifts. Also, the self-consistent field has caused a section of the cloud on the planetward side to maintain the coincidence between the two boundaries, which would not occur for drifts in the external field only. Thus it may be possible to explain the existence of both the dispersive and dispersionless boundaries with the combined effects of substorm injection and the self-consistent field, although a detailed matching of such a theory with the observations has not been attempted.

In general it is difficult to interpret features such as those in Plate 9 from one spacecraft passage through a system because spatial and temporal variations cannot be distinguished. For Earth-orbiting satellites, a statistical study

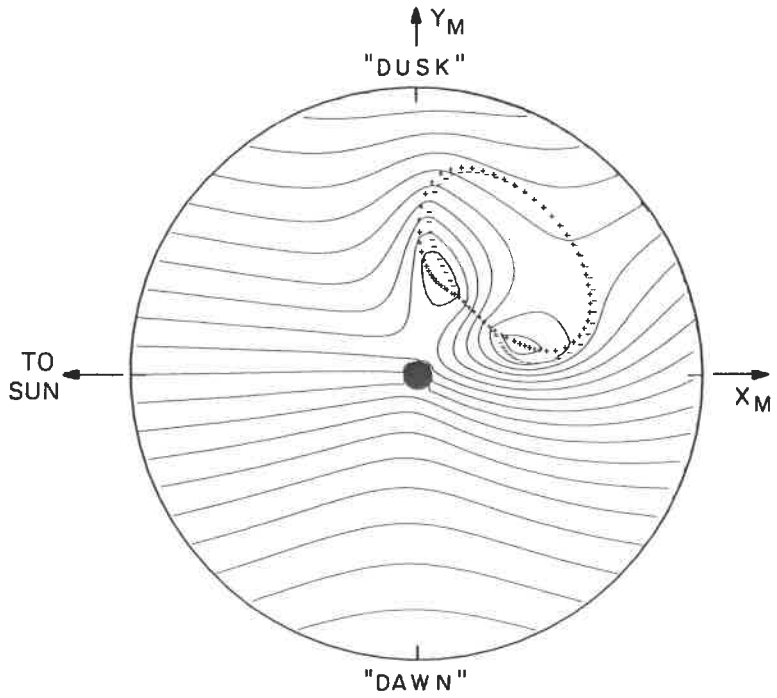

Fig. 14. Electrostatic potential contours at 4 hr after injection of a plasma cloud that started initially as a circle with coincident proton (+) and electron boundaries (−). The vertical and horizontal axis in this figure are the same as in Fig. 4.

of many such data sets typically is needed (see e.g., Mauk and Meng 1983; Fairfield and Vinas 1984). The Voyager 2 trajectory provided only a few hours of data from the inner Uranian magnetosphere, and this may or may not be representative of the important plasma dynamics. As we have seen, the data cannot be easily explained by either the Alfvén layer or injection boundary models, and other mechanisms might need to be considered.

IV. PLASMA SOURCES AND SINKS

Sources for the Warm Ions

Using 3 days as a reasonable estimate of the plasma residence time, one can calculate the plasma source strength for the hot and warm plasma components (see McNutt et al. 1987). The number of ions in a flux shell 1 L in width is given by $N = 2\pi R_U^3 L^2 n$ (Siscoe 1978*b*), where the ion number density n is taken to be constant throughout a flux shell (appropriate for the very subsonic plasma at Uranus). A density of 1 cm^{-3} for the warm component and 0.2 cm^{-3} for the hot component at $L = 5$ gives $N_{warm} = 2.6 \times 10^{30}$ and $N_{hot} = 5.3 \times 10^{29}$ (in both cases assuming a source region extending from $L \sim 5$ to ~ 6). A residence time of 3 days yields a source strength of 2×10^{24} s^{-1} for the hot protons and 8×10^{24} s^{-1} for the warm protons. Because the density and residence time are both rapidly decreasing functions of L, the inaccuracies arising from assuming $5 < L < 6$ instead of integrating throughout the magnetosphere are small. The derived rates are a small fraction of the 5×10^{28} hydrogen atoms that escape from the atmosphere of Uranus each second (Broadfoot et al. 1986).

The source of the warm ions is probably the neutral hydrogen corona or the ionosphere of the planet. The density and temperature of the warm component are nearly constant throughout the region where they are observed, except for a few narrow density spikes. This constancy argues for a local source, because adiabatic transport would otherwise result in an $L^{-8/3}$ dependence (see the discussion following Eq. (1) above). The difficulty with a local source, however, is that locally ionized protons would be formed with energy equal to the rotational energy where they are formed ($\sim$ 1 eV). Thus a local source must not only provide $\sim 10^{25}$ protons s^{-1}, but it must also accelerate them to energies of order 10 eV. The first pertinent question is whether the neutral hydrogen cloud can provide 10^{25} protons s^{-1}. The neutral atomic hydrogen density in the exosphere at $L = 5$ unfortunately is not well known. Applying the model of Shemansky and Smith (1986) to Voyager UVS observations yields a value of $\sim$70 cm^{-3} at $L = 5$ (D. E. Shemansky, personal communication, 1986); however, this value is associated with large uncertainties, and the range of possibilities may extend from $\sim$10 cm^{-3} to 100 cm^{-3}. Although this range of densities is used in the discussion below, the reader

should be aware that recent calculations by Herbert (1988*a*) impose upper limits of a few hydrogen atoms cm^{-3} on the night side and tens of hydrogen atoms cm^{-3} on the day side.

At 100 eV the electron impact ionization rate is 1.0×10^{-8} cm^3 s^{-1} (Lotz 1967). Combined with an electron density of 1 cm^{-3} at a temperature of 100 eV, a density of 10 to 100 atoms cm^{-3} yields a source strength of between 1×10^{23} and 1×10^{24} s^{-1} per unit L from electron impact ionization. Photoionization is a less important process in the inner magnetosphere, out to L-shell values of ~10 to 15, where it becomes comparable to impact ionization owing to decreasing electron densities. Considering the qualitative nature of these estimates, the source strength associated with impact ionization of the neutral cloud hydrogen can probably supply the observed density of protons; however, this source also requires a mechanism to accelerate the newly created ions to the observed energies (around 10 eV). Selesnick and McNutt (1987) proposed that adiabatic compression resulting from sunward convection is sufficient to explain the elevated temperature of ions picked up from the neutral hydrogen cloud. In this scenario, the neutral hydrogen source is continually ionized by electron impact ionization, and the resulting (cold) ions (which are initially tailward of their observation point) are then convected sunward and adiabatically heated sufficiently for their observation by the PLS instrument. This model generates the required heating of the ions and resultant energy spectra that agree qualitatively with those observed. Thus it is plausible that the source of the warm ions is ionization of the neutral hydrogen cloud. Ionospheric injection could also provide a source for the warm ions. Cheng (1987) estimated the ionospheric proton source between $L = 4.6$ and $L = 5.5$ to be 5.7×10^{23} s^{-1}, so the ionosphere could be a significant source for the warm ions.

Sources for the Hot Ions

The hot ion component probably convects inwards from the magnetotail, reaching its high energies via adiabatic compression over these distances. The constant flux-tube content η for the hot and intermediate ions outside of L values of ~6 also argues for a tail source (cf. Fig. 11). If the solar wind were the plasma source, then conservation of the first adiabatic invariant from the solar wind, where $B = 0.1$ nT (R. P. Lepping, personal communication, 1986) and $T_{ion} = 0.5$ eV (from Voyager 2 PLS measurements in the upstream solar wind), to the magnetosphere at $L = 5$ results in $T_{ion} = 1$ keV in this region. The total number of solar wind particles with speed V_{SW} and number density n_{SW} impinging on a magnetosphere of effective radius R_M is $\pi R_M^2 n_{SW} V_{SW}$. If one assumes that the efficiency of plasma transport across the magnetopause of 10^{-3} and that the solar wind number density is 0.04 cm^{-3} (Bagenal et al. 1987), with other values as quoted above, the solar wind source could provide 10^{25} s^{-1}. This is close to the requirements for the hot ions.

However, the fact that Krimigis et al. (1986*a*) found no helium at energies > 600 keV $nucleon^{-1}$ argues *against* a solar wind source. It is surprising that the solar wind is not an important source, given the above estimates of probable source strengths, but the composition at high energies is a strong argument against a significant solar wind contribution to the hot ion component.

Another possible plasma source for the hot ions and electrons is the ionosphere in the auroral regions of the planet. Energetic protons precipitating into an atmosphere of molecular hydrogen produce a population of secondary electrons with a mean energy of 20 to 40 eV (Kuyatt and Jorgensen 1963). These electrons have sufficient energy to escape the ionosphere; they pull cold protons with them along the magnetic field lines, to maintain charge neutrality. The protons acquire energy from the centrifugal potential equal to the local rotational energy (Hill et al. 1974). This is about 13 to 20 eV for $L = 20$ to 25, which is the location of the nightside auroral region (15 to 20° in diameter and centered on the south magnetic pole according to Broadfoot et al. [1986]). Adiabatic heating can increase these energies to 830 to 2500 eV if the protons convect inward to $L = 5$. Thus, ionospheric protons can be heated to energies consistent with those observed by the PLS experiment. The secondary electrons, which are also heated to a few keV as they convect inwards to $L = 5$, could be a source of the hot electrons observed on the night side of the planet (Sittler et al. 1987; Bridge et al. 1986).

Plasma Sinks

Following the above discussion of possible plasma sources, it is appropriate to consider some of the possible plasma sinks. These include satellite sweeping, absorption of plasma by the rings, convection to the dayside magnetopause, and precipitation losses. Losses due to charge exchange with the neutral hydrogen cloud may be important for ions; electron impact ionization is a likely energy sink for electrons.

Satellite sweeping is probably unimportant for the low-energy plasma because gradient drift times are long compared to convection times. The plasma edges were initially thought to be associated with Miranda because they are roughly coincident with the minimum L-shell of Miranda's orbit (cf. Fig. 3). The large offset between the magnetic dipole and rotation axes has the result that Miranda intersects field lines from $L = 5$ to $L = 20$, with the largest amount of time spent at lower L-shells. Because the absorption is largest and transport slowest at the minimum L-shell, a sharp boundary could form. One of the problems with this scenario is that the edges are not symmetric; the location of the edge was at $L = 5.3$ during the inbound pass and at $L = 4.8$ during the outbound pass, rather than at the predicted value of $L = 5.0$ both inbound and outbound. It could be argued that the field model is at fault, but the depletions in the fluxes of the high-energy particles, which can realistically be presumed to be due to absorption by Miranda, are sym-

metric in L using the field model; they occur at $L = 5.2$ both inbound and outbound (Stone et al. 1986). The PLS boundaries cannot be explained as a simple L-shell effect even using the more accurate Q_3 model of the magnetic field.

Another difficulty is that Miranda is at its minimum L-shell only in limited ranges of magnetic longitude (cf. Sittler et al. 1987, Fig. 11). Thus, sweeping up of the particles can form a sharp boundary only if the plasma drifts fast enough azimuthally so that it reaches the sweeping regions before it is convected inward past Miranda's orbit. However, gradient drifts for particles in the PLS energy range are not fast enough to exceed convection times inward past Miranda (cf. Sittler et al. 1987, Fig. 10). One might also argue that convection is slow and transport is by radial diffusion; unfortunately, diffusion would not create sharp boundaries, but would instead produce a gradual drop in density inward from a peak located near $L = 6$. It is therefore highly improbable that the sharp drop-outs are associated with Miranda, or that sweeping by satellites is an important loss process.

The drop in thermal electron temperature from 1709 to 1715 UTC may be associated with cooling and absorption by ring material. The offset in the thermal electron signature toward the day side of the ring event seen in the plasma wave data (Gurnett et al. 1986) may be due to a sudden time-dependent increase in convection of the plasma from the night side to the day side possibly associated with a substorm. Precipitation losses will occur whenever there is pitch angle scattering by plasma waves. Whistler mode waves might be important for scattering electrons into the loss cone; subsequent precipitation could then remove the electrons. Whistler-mode waves were observed by the PWS instrument (Gurnett et al. 1986), but their resonance energies were generally more than 50 keV, much higher than energies of electrons observed by PLS. Coroniti et al. (1987) reported strong pitch angle scattering for electrons with $E > 3$ keV from 2000 to 2100 UTC. During this period, the electron fluxes peaked at energies above the 6 keV high-energy limit of the PLS instrument, and these higher-energy electrons probably provided the free energy for the enhanced wave amplitudes observed by the PWS instrument.

The neutral hydrogen cloud is a potentially important sink for protons via resonant charge exchange interactions (originally noted by Krimigis et al. 1986*a*) and for electrons via impact ionization. Sittler et al. (1987) consider this process in detail, and conclude that resonant charge exchange is probably a major sink for the protons, and that the neutral hydrogen densities must be <200 cm^{-3} at $L = 5$. However, electron impact ionization is not found to be an important energy sink for the electrons. As mentioned above, Herbert (1988*a*) has also modeled the convection of the hot plasma component through the magnetosphere, incorporating charge exchange loss with the neutral hydrogen in the corona, and concluded that upper limits for the H density

at $L = 5$ were several H cm^{-3} on the night side and tens of H cm^{-3} on the day side.

V. THE MAGNETOTAIL AND PLASMA SHEET

As Voyager traversed the night side outer magnetosphere, the PLS instrument repeatedly observed enhancements of electron and ion fluxes (Bridge et al. 1986). These enhancements were due to passages of the spacecraft into or through the Uranian plasma sheet. The plasma sheet observations are well organized in solar magnetospheric coordinates. In this system, the $\mathbf{X}_{SM}$ axis is toward the Sun, and the $\mathbf{Z}_{SM}$ axis is defined so that the planet's magnetic dipole axis lies in the $\mathbf{X}_{SM} - \mathbf{Z}_{SM}$ plane, with the magnetic dipole moment having a negative $\mathbf{Z}_{SM}$ component. Figure 15 shows the trajectory of Voyager 2 projected onto the solar wind magnetospheric $\mathbf{Y}_{SM} - \mathbf{Z}_{SM}$ plane (a cross section of the tail as viewed from the Sun) and onto the $\mathbf{X}_{SM} - \mathbf{Z}_{SM}$ plane (the noon-midnight plane containing the solar wind flow vector and the planetary magnetic dipole). The portions of the trajectory with enhanced total electron flux (in the energy range 140 eV to 6 keV) are indicated.

The observations made on 25 January are consistent with a simple model of the plasma sheet represented by the shading in Fig. 15. The plasma sheet has a full thickness of about 10 R_U near the midnight meridian that increases to about 15 R_U at the sides, and its central plane deviates from the magnetic equatorial plane to become parallel to the solar wind flow at tailward distances beyond 10 to 15 R_U. The plasma sheet is raised above the solar magnetosphere $\mathbf{X}_{SM} - \mathbf{Y}_{SM}$ plane as a result of the dipole tilt away from the $\mathbf{Z}_{SM}$ axis. Note that the drop-out on 24 January at 2250, discussed above, probably corresponds to the high-latitude boundary of the plasma sheet at $L \approx 18$, above which the spacecraft entered open field lines (see above). The plasma edges discussed above could also be interpreted as the inner edges of the plasma sheet. The configuration and dimensions of this model correspond qualitatively to a suitably scaled average model of the terrestrial plasma sheet.

It is worth emphasizing a fundamental difference between the Uranian magnetotail and that of the Earth. Owing to the near-alignment of the Uranian spin axis with the solar wind flow direction, the tail structure does not wobble up and down as at Earth or Jupiter, but instead rotates in space approximately about the $\mathbf{X}_{SM}$ axis. Nonetheless, the actual dipole tilt angle measured from the $\mathbf{Z}_{SM}$ axis in the rotating solar magnetospheric coordinate system varies in the range only from 22° to 38°. The values of this tilt are not unlike those of the Earth, which never exceed 35°. As Voigt et al. (1987) point out, it is the Earth-like tilt angles at Uranus which lead to the development of an Earth-like dipolar magnetic tail, with lobes separated by a cross-tail current and plasma sheet (Ness et al. 1986; Behannon et al. 1987). A more detailed model of the magnetotail, based on magnetic field observations (Behannon et al.

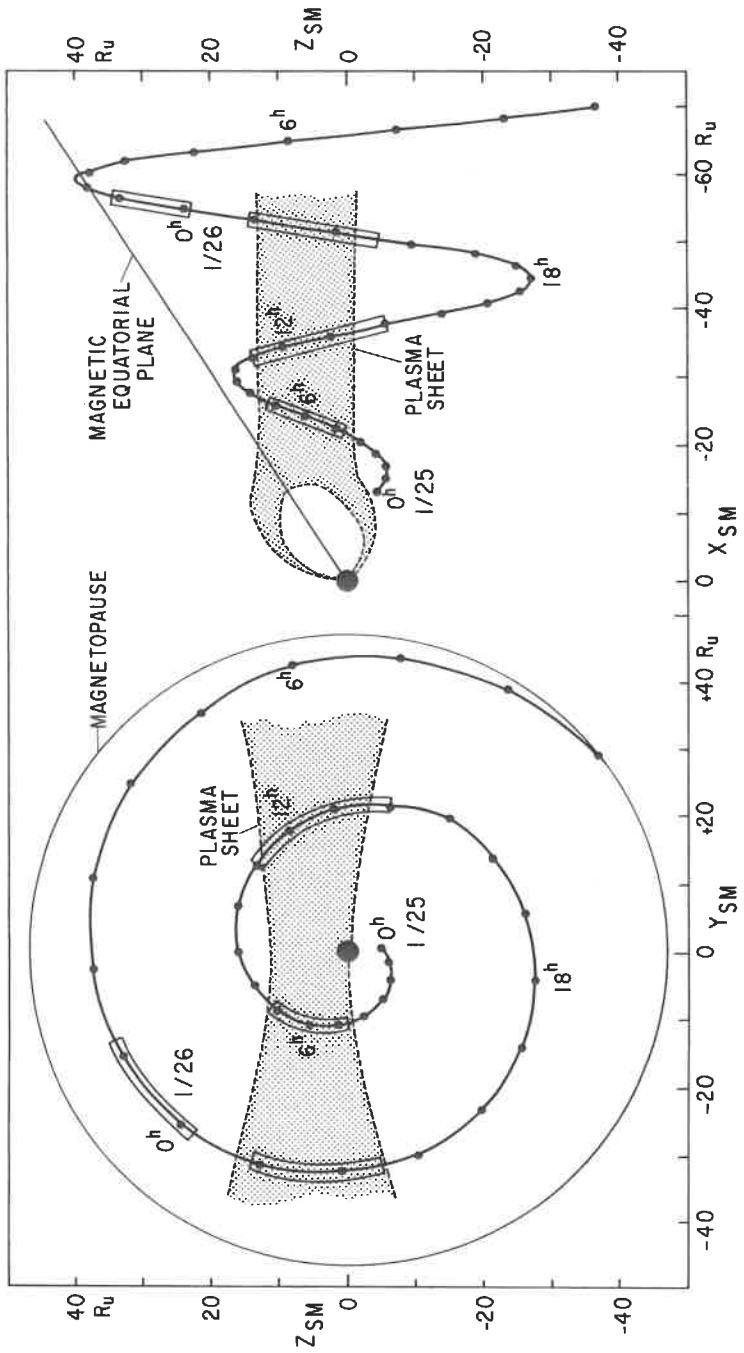

Fig. 15. Trajectory of Voyager 2 in solar magnetospheric coordinates (figure after Bridge et al. 1986). Left panel: $Y_{SM} - Z_{SM}$ plane; right panel: $X_{SM} - Z_{SM}$ plane. Positions of the spacecraft are marked every hour. Periods of enhanced electron intensities associated with the plasma sheet are shown in boxes; the shading corresponds to a model of the plasma sheet (see text). The inner edge of the plasma sheet in the right panel is speculative, and the structure of the inner magnetosphere is not shown.

1987), suggest an asymmetry in the shape and thickness of the sheet, with a significantly smaller thickness on the side of the tail on which the first and third crossings of the sheet occurred, in keeping with the predictions of Voigt et al. (1983). Pressure balance within the plasma sheet is maintained predominantly by protons and electrons with energies below 6 keV, in contrast to the situation at Jupiter, where more energetic ions are responsible for pressure balance in the Jovian magnetotail (Lanzerotti et al. 1980). A thorough discussion of observations in the magnetotail can be found in Behannon et al. (1987).

The observations made after 0 hr on 26 January are no longer consistent with the model described above, in that the plasma sheet was observed between 0 and 1 hr, considerably above its expected position, and a crossing was not observed around 6 hr, where it was expected. There is a variety of reasons why the simple model may break down at these distances, including proximity of the magnetopause, changes of the configuration beyond 55 R_U (e.g., as a result of the breakdown of co-rotation), and the possibility of a major temporal change associated with a change in solar wind direction.

VI. OUTBOUND MAGNETOSHEATH AND SOLAR WIND OBSERVATIONS

As is evident from Fig. 1, Voyager was in the tailward magnetosheath of Uranus for about 72 hr, or slightly more than 4 Uranian days. Oscillations in plasma properties, with periods ranging from tens of minutes to the Uranian rotation period, were observed. In this time interval, the spacecraft observed sheath flow that passed over all magnetic latitudes because of the orientation of the spin axis of Uranus. Thus these data provide a unique opportunity to search for features in the plasma parameters that vary with magnetic latitude or with planetary rotation (Richardson et al. 1988). Figure 16 shows the **R**-component of velocity in the solar equatorial **RTN** system, where **R** is radially away from the Sun, **T** is parallel to the solar equatorial plane and positive in the direction of planetary motion and **N** completes the right-handed system. The data plotted are running 1 hr averages of velocities obtained from PLS *M*-mode spectra. Data are shown only when the spacecraft is in the sheath; this serves to eliminate confusion arising from velocity variations at outbound bow shock crossings. Decreases in the velocity occur at decimal days 26.9, 27.6, 28.4, 29.1 and 30.6. The first 4 decreases are about 17 hr apart (about one Uranian day), then a cycle is missed but the last decrease is also in phase. The decreases at 26.9 and 27.6 are both entirely in the sheath. The onset of the decreases at 28.4 and 29.1 are also clearly due to variations in the sheath flow; the recovery of the velocity from these decreases is not observed because Voyager passes into the solar wind before this occurs. The last decrease at 30.6 is bounded on both sides by bow shock crossings; however the maximum and minimum velocities observed are con-

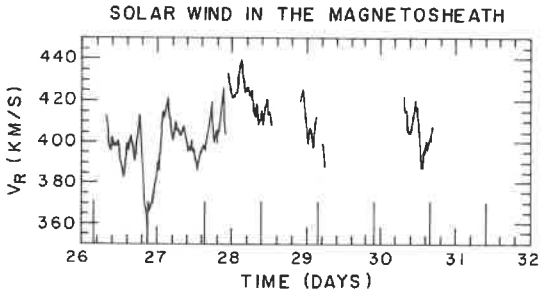

Fig. 16. Running 1-hr averages of the *R*-component of solar wind velocity in the magnetosheath. The solid lines show where the maximum effects from reconnection should occur assuming that the interplanetary magnetic field is in the $\hat{T}$ direction.

sistent with the other decreases, so this may be a similar signature. The average amplitude of the velocity decreases is approximately 30 km s^{-1}, 7.5% of the total radial velocity. The average width of the velocity decreases is about 6 hr. The variation of velocity with time is neither smooth nor sinusoidal; the boundaries of the decreases are usually sharp.

Although the limited quantity of data precludes firm conclusions, Richardson et al. (1988) hypothesized that the velocity decreases are associated with dayside reconnection. The cause of the velocity decreases would be drag on the reconnected flux tubes, which are coupled via Birkeland (field-aligned) currents to the ionospheric plasma. Reconnection can occur on the dayside magnetopause when the interplanetary magnetic field (IMF) and planetary magnetic field are antiparallel. The planetary field is known (Ness et al. 1986), but the IMF direction is not known when Voyager is in the magnetosheath. At large heliospheric distances the IMF is for the most part tangential (in the $\pm$**T** direction), although large deviations occur and the polarity can switch at sector boundaries. Richardson et al. (1988) used a tangential field to calculate the merging geometry, and further assumed that the effects of reconnection propagate down the magnetosheath at the solar wind velocity, which was about 430 km s^{-1} both before and after the encounter (Bridge et al. 1986). The times at which the maximum effect of reconnection on the magnetosheath should be observed if the field is in the +**T** direction (solar wind towards sector) are shown by the solid vertical lines in Fig. 16. These locations correlate well with the location of the velocity decreases. Since the magnetic field data from the sheath at the times of the velocity decreases is usually consistent with the IMF in the +**T** direction, reconnection seems to be a viable mechanism for producing the velocity decreases. This result is not very sensitive to propagation speed through the magnetosheath because the time between dayside reconnection and observations in the tail is only a few hours.

In addition to the periodicity in the velocity which occurs on the time

scale of a planetary rotation, plasma oscillations also occur on much shorter time scales (Richardson et al. 1990). Large fluctuations in the density occur episodically throughout the outbound sheath crossing. An example is given in Fig. 17, which shows the plasma density, thermal speed and the *T* component of velocity in a 3.6-hr period of day 27. The plasma fluctuations exhibit density increases of a factor of up to 5 that are anticorrelated with the plasma thermal speed (temperature). The plasma flow direction is also correlated with these fluctuations, with the *T* component of velocity changing by more than 100 km s^{-1}. These oscillations occur during periods when the magnetic field direction and magnitude are fluctuating rapidly. Although these waves have time and distance scales placing them in the MHD regime, their characteristics are not compatible with any known solution of the MHD equations. Richardson et al. (1990) suggest that these fluctuations are produced

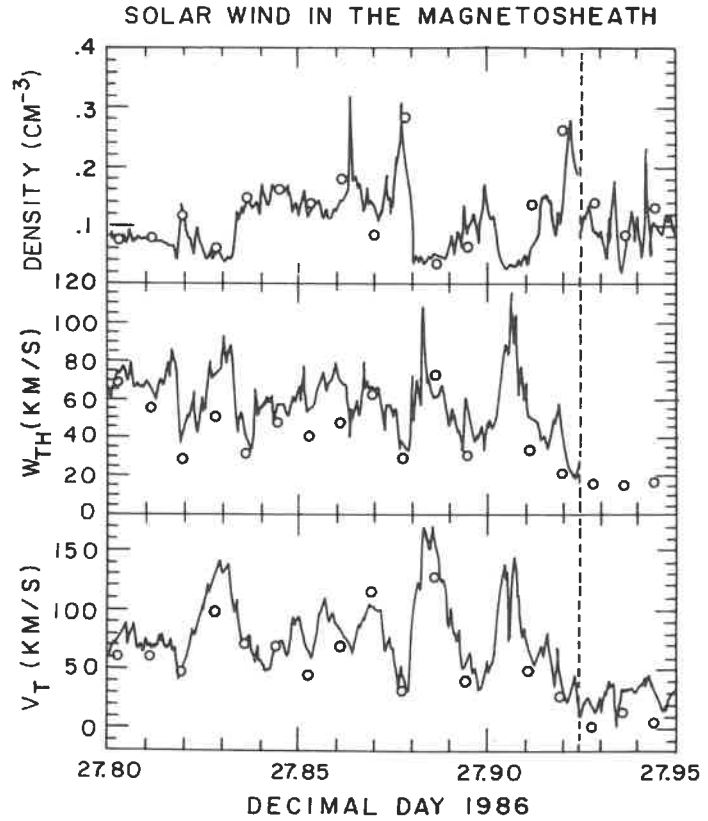

Fig. 17. Plasma density, thermal speed and the *T*-component of solar wind velocity on 27 January 1986. The dashed line shows the location of the bow shock. The solid lines show data from the PLS *L*-mode, the circles data from the *M*-mode.

by the solar wind interaction with the magnetosphere at the bow shock, but the physics governing the production and propagation of these fluctuations is not understood.

Plasma waves were also detected in the solar wind downstream from Uranus when the spacecraft is connected to the Uranian bow shock by the IMF (Zhang et al. 1990). These are Alfvénic and/or fast-mode waves with frequencies of 10^{-3} Hz, which are right-hand polarized and propagate nearly parallel (or anti-parallel) to the magnetic field away from the bow shock. Near Uranus the waves have amplitudes $\delta B/B$ equal to unity, but the amplitudes decay as the spacecraft moves downstream from Uranus. These waves are probably generated by a resonant ion beam instability near the nose of the bow shock.

VII. INBOUND BOWSHOCK

As the average magnetic field, plasma density and temperature of the solar wind decrease away from the Sun, the Mach numbers of the flow increase, reaching average values > 10 at Uranus's orbital distance of 19 AU. Not unexpectedly, Voyager 2 crossed a high Mach number bow shock on the day side of the Uranian magnetosphere (Bagenal et al. 1987). Figure 18 shows the profiles of the magnetic field magnitude, the components of the plasma flow velocity (in solar equatorial **RTN** coordinates), and the ion and electron densities and temperatures measured through the shock. These profiles of plasma measurements through the Uranian bow shock show the transition from cold, tenuous solar wind plasma streaming in a radial direction, to hot, compressed magnetosheath plasma, deflected tangentially around the magnetosphere. In Table I, we tabulate the values of plasma parameters in the upstream and downstream regions, plus various Mach numbers and scale lengths derived from these basic parameters. The 5 Mach numbers ($\mathbf{M}_S$, $\mathbf{M}_P$, $\mathbf{M}_A$, $\mathbf{M}_{MS}$, $\mathbf{M}$) compare the plasma flow speed $\mathbf{V}$ to the local sound speed C_S, ion thermal speed w_{th}, Alfvén speed $\mathbf{V}_A$, fast-mode speed $\mathbf{V}_{fms}$, and an effective ion acoustic speed as defined in the table. Clearly, this is a high Mach number, high β shock (β is the ratio of plasma pressure to magnetic field pressure).

Although the average conditions on either side of the shock are consistent with the Rankine-Hugoniot (MHD) relations for a stationary, quasi-perpendicular shock (Bagenal et al. 1987), the detailed measurements reveal structure in the transition region as well as considerable variability in the downstream magnetosheath plasma. The transition region has finite thickness and exhibits certain features that are both reminiscent of the Earth's bow shock as revealed in detail by the ISEE spacecraft and consistent with current theoretical models of high-Mach-number quasi-perpendicular shocks (Leroy 1983; Wu et al. 1984; Scudder et al. 1986*a,b,c*). The magnetic field, ion temperature, and plasma density all began to increase at about 0716 UTC, 15

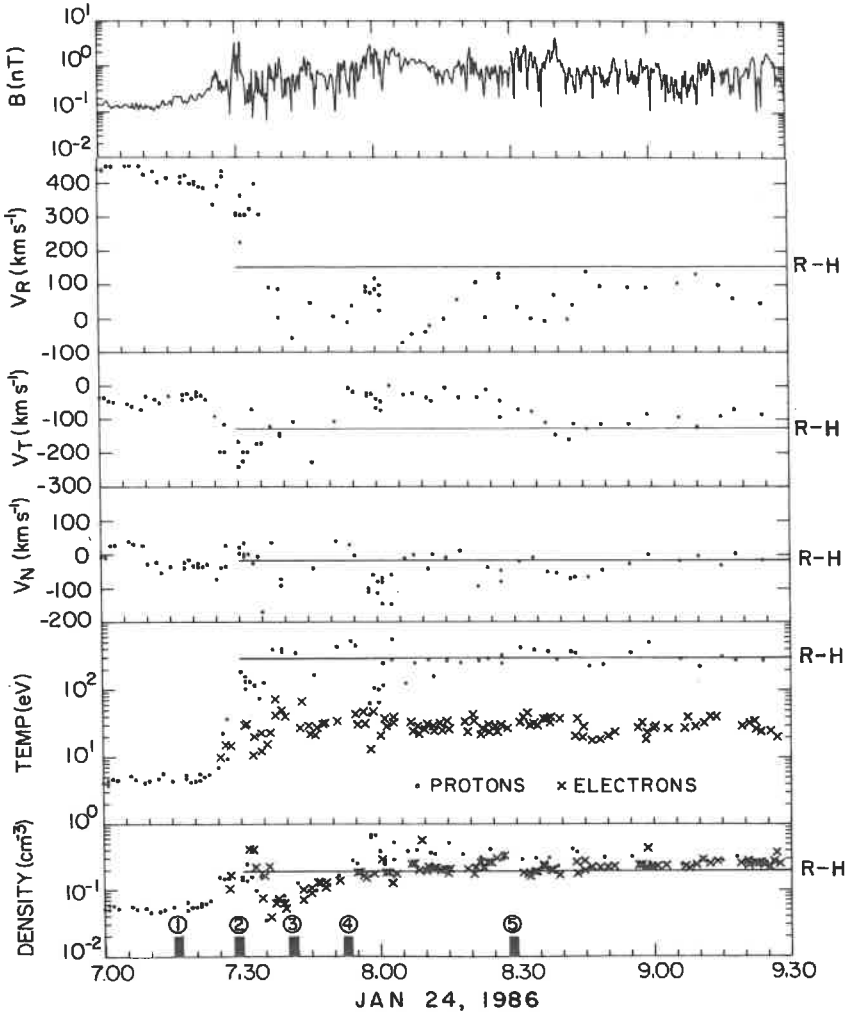

Fig. 18. Profiles of magnetic field and plasma parameters vs time as Voyager 2 crossed the Uranian bow shock. The values of these parameters predicted by the Rankine-Hugoniot (*R-H*) relations are shown by horizontal lines. The dots show ion measurements and the crosses give electron density and temperature.

min before the sharp transition (the ramp) at 0729. With the spacecraft moving at 15.9 km s^{-1}, the 15-min interval would imply that the upstream extension of the bow shock (generally called the "foot") has a width of 14,300 km (0.56 R_U) if the shock were stationary. The width of the foot is expected to be a fraction of the effective ion gyroradius $r'_{gi} = V_{sw}/\Omega_{ci}$, which is 23,000 km (0.9 R_U) for the Voyager 2 measurements in Table I. For a perpendicular shock, Schwartz et al. (1983) derived a foot width of 0.7 r'_{gi} (0.63 R_U). The

TABLE I
Observed Plasma Parameters at the Uranian Bow Shock[a]

	Definition	Upstream[b]	Downstream
n, cm^{-3}		0.05	0.25
T_i, eV		4.2	300
T_e, eV		<3.	30
T_c, eV		<2.6	22
T_h, eV		14.[c]	200
V, km s^{-1}		450	150
B, nT		0.19	0.7
β_e	$8\pi nkT_e / B^2$	<1.5	4.7
β_i	$8\pi nkT_i / B^2$	2.1	47
$\beta_T = \beta_e + \beta_i$		<3.6	52
$M_S = V/C_s$	$C_s^2 = kT_e/m_p$	27	2.8
$M_p = V/w_{th}$	$w_{th}^2 = 2kT_i/m_p$	16	0.6
$M_A = V/V_A$	$V_A^2 = B^2/4\pi n\, m_p$	23	4.3
$M_{MS} = V/C_{fms}$	$C_{fms}^2 = C_s^2 + V_A^2$	17	2.3
M	$M^2 = m_p V^2/k(T_e + T_i)$	17	0.8
r_{ge}, km		21	16
r_{gi}, km		1050	2210
c/ω_{pe}, km		24	11
c/ω_{pi}, km		1030	470
$r'_{gi} = V/\Omega_{ci}$, km		23000[d]	3500[e]

[a]Table from Bagenal et al. 1987.
[b]0700–0716 UTC.
[c]Olbert 1982.
[d]$V_{sw} / (\Omega_{ci})_{upstream}$
[e]$V_{sw} / (\Omega_{ci})_{downstream}$

15-min duration of the foot suggests that the shock was slowly moving toward the spacecraft and away from Uranus at the time of the shock crossing, foreshortening the shock. The upstream foot of a shock is generally attributed to the presence of ions that are reflected at the shock (Paschmann et al. 1982). The high energy-per-charge resolution ion spectrum (M-mode) obtained at 0728 UTC just before the ramp shows features on either side of the main population, which may indicate the presence of such ions.

After the foot, the magnetic field increased rapidly to a maximum value B_{max} of 3.2 nT before oscillating about an average downstream value of $B_d \sim 0.7$ nT. This gives a value for the overshoot O , $(B_{max} - B_d) / B_d$ of 3.7. The duration of the ramp was about 15 s, corresponding to a distance of 225 km for a stationary shock. Early theoretical studies suggested the ramp should have a width of about an ion inertial skin depth c/ω_{pi}. The width observed at Uranus is only 0.2 c/ω_{pi} (Table I), which is very similar to the ramp width reported by Scudder et al. (1986*a*). The overshoot is characteristic of supercritical shocks where the value of the overshoot O is thought to increase with M_{MS}. Russell et al. (1982) has shown that observations of the

bow shocks of Venus, Earth, Jupiter and Saturn, where the observed M_{MS} was $\lesssim$11, generally conform to such a trend. After the overshoot both the magnetic field magnitude and plasma density dropped briefly to values slightly below the ambient solar wind values. Voyager 2 crossed this deep undershoot in about 5 min, corresponding to a width of ~4500 km for a stationary shock. Because of the variable conditions behind the shock, it is difficult to distinguish subsequent (damped) oscillations from background fluctuations. However, the plasma density profile in Fig. 18 suggests the first phase of the oscillation was completed between 0745 and 0800 UTC, corresponding to a wavelength of 1 to 2 times the upstream effective gyroradius $r'_{gi} = V_{sw}/(\Omega_{ci})_U$ (cf. Scudder et al. 1986*a*) or about 10 times the downstream $r'_{gi} = V_{sw}/(\Omega_{ci})_D$ (where V_{sw} is the upstream solar wind speed in both cases). During the undershoot the plasma velocity showed strong deviations from a simple tangential deflection of the flow. The radial component V_R not only decreased but turned negative (sunward) for brief periods. The existence of negative V_R may be consistent with the ion dynamics revealed in simulations of high Mach number shocks, or might suggest the shock is not in fact planar or stationary. Thus the Voyager 2 inbound bow shock observations exhibit features consistent with a foot, an overshoot, reflected ions and downstream oscillations, all of which are qualitatively expected of a high Mach number supercritical shock.

VIII. SUMMARY

The Voyager 2 encounter with Uranus revealed a number of unexpected features. These plasma features mark the Uranian magnetosphere as uniquely different from those of Jupiter and Saturn at this epoch. The most unexpected discovery, in terms of comparative magnetospheric physics, is that solar-wind-driven convection and planet-driven co-rotation are decoupled at Uranus (Vasyliunas 1986; Selesnick and Richardson 1986; Hill 1986). This decoupling occurs because of the unique orientations of the planetary spin axis with respect to the solar wind flow direction, and of the magnetic dipole axis with respect to the spin axis. As a result of these orientations, convection penetrates deep into the inner Uranian magnetosphere, sweeping out the magnetospheric plasma on relatively short time scales, and preventing the formation of a dense plasmasphere.

The low-energy plasma in the magnetosphere consists of protons and electrons, with no significant heavy ion contribution from the moons, presumably because of the rapid convective time scales and the extreme tilt of the magnetic dipole axis. The plasma electrons and ions exhibit both a thermal component (with temperatures of tens of eV) and a hot component (with temperatures of a few keV). The source of the thermal component is either the planetary ionosphere or the neutral hydrogen corona surrounding Uranus. Both of these sources produce cold plasma which must be subsequently

heated to reach the observed energies. Heating due to adiabatic compression associated with sunward convection is a plausible explanation for the energization of the warm component.

The hot component is almost certainly convected in from the magnetotail, with probably an ionospheric source. The plasma edges that exclude the hot ions from a region inside an L-shell value near 5 are thought to be due to a quasi-steady Alfvén layer, although some features in the inner magnetosphere are more characteristic of a time-dependent injection boundary. However, there are aspects of the plasma data that cannot be easily explained by either of these models, and no totally satisfactory model of the inner magnetospheric region currently exists.

Uranus also possesses a well-developed magnetotail and plasma sheet similar in many respects to those of the Earth. Outbound there is some evidence for periodic velocity variations in the magnetosheath which may be signatures of reconnection. The outbound magnetosheath also has regions in which large plasma density and flow oscillations occur on a time scale of several minutes. The bow shock observed inbound is a high Mach number quasi-perpendicular shock and shows detailed structure similar to that seen at the Earth.

The combination of the orientation of the Uranian rotation axis with respect to the solar wind direction and of the Uranian magnetic dipole axis with respect to the rotation axis is unique in the solar system. Because of this, the exploration of the magnetosphere of Uranus by Voyager 2 has provided a considerable increase in understanding of comparative magnetospheric processes, confirming preconceived notions in some instances, but prompting re-examinations in others. In particular, the Uranian magnetosphere is neither convection-dominated nor co-rotation-dominated, but a unique combination of both. Undoubtedly, many interesting results will be forthcoming as the Voyager 2 data sets are more thoroughly analyzed. Direct exploration of the magnetosphere of Uranus has once more demonstrated the crucial role of observation in understanding physical processes in the large-scale plasma systems occurring in Nature.

ENERGETIC PARTICLES AT URANUS

ANDREW F. CHENG, S. M. KRIMIGIS
The Johns Hopkins University

and

L. J. LANZEROTTI
AT&T Bell Laboratories

This chapter reviews the energetic particle measurements by the Low Energy Charged Particles and Cosmic Ray instruments on the Voyager 2 spacecraft in the magnetosphere of Uranus. Upstream ion events were observed outside the Uranian bow shock, probably produced by ion escape from the magnetosphere. However, no energetic neutral particle fluxes were observed, placing an upper limit of $< 60\ cm^{-3}$ average neutral hydrogen density inside 6 R_U. Evidence of Earth-like substorm activity was discovered within the Uranian magnetosphere. A proton injection event was observed within the orbit of Umbriel and proton events were observed in the magnetotail plasma-sheet boundary layer that are diagnostic of Earth-like substorms. The magnetospheric composition is totally dominated by protons, with only a trace abundance of H_2^+ and no evidence for He or heavy ions; the Uranian atmosphere must be the principal plasma source. Energetic particle bombardment of any methane-bearing ice surfaces would blacken these surfaces in geologically short times, but photosputtering and meteoroid bombardment are also effective mechanisms for erosion of water-ice surfaces on the Uranian satellites. Phase-space densities of medium energy protons show inward radial diffusion and are quantitatively similar to those observed at Earth, Jupiter and Saturn. These results and plasma wave data suggest the existence of structures analogous to Earth's plasmasphere and plasmapause. Electron phase-space densities suggest the existence of local sources of energetic electrons. Particle absorption signatures are also observed for ions and electrons at the minimum L-shells of the inner satellites, but it is not yet

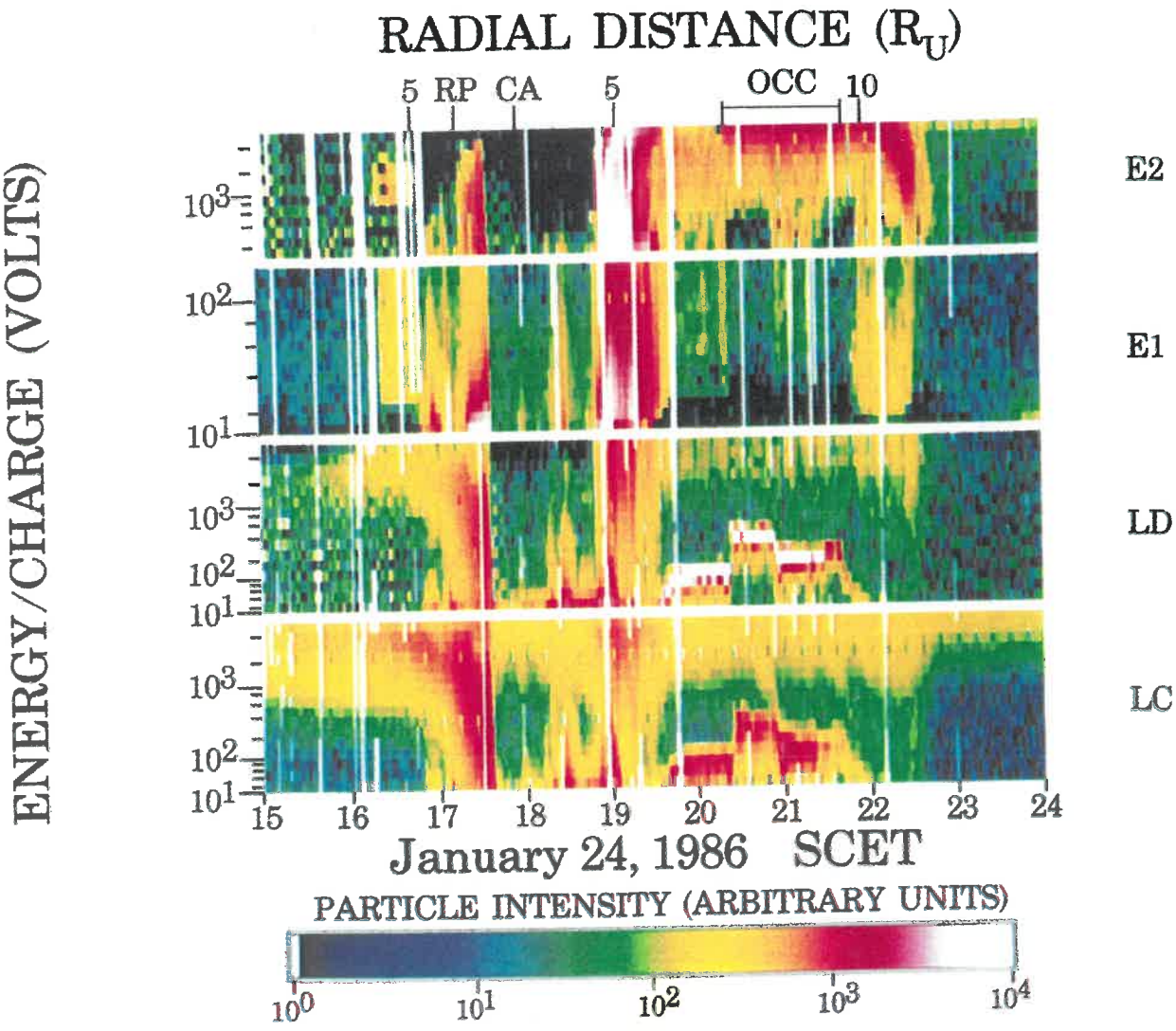

Plate 1. Color energy-time spectrogram of the PLS ion and electron currents from 1500 to 2400 UTC on 24 January 1986 (Plate after Sittler et al. 1987). The horizontal color bar gives the color code used to define relative particle flux. The designation RP on the upper horizontal axis denotes the time of the crossing of the ring plane, the designation CA denotes the time of closest approach to the planet, and the designation OCC denotes the time of solar occultation. (See the chapter by Belcher et al.)